Comparisons of ground-based tropospheric NO2 MAX-DOAS measurements to satellite observations with the aid of an air quality model over Thessaloniki area, Greece

Theano Drosoglou[1], Alkiviadis F. Bais[1], Irene Zyrichidou[1], Natalia Kouremeti[1,2], Anastasia Poupkou[1], Natalia Liora[1], Christos Giannaros[1], Maria Elissavet Koukouli[1], Dimitris Balis[1], Dimitrios Melas[1]

[1]Laboratory of Atmospheric Physics, Aristotle University of Thessaloniki, Thessaloniki, 54124, Greece
[2]Physikalisch-Meteorologisches Observatorium Davos, Dorfstrasse 33, CH-7260 Davos Dorf, Switzerland

Correspondence to: Theano Drosoglou (tdroso@auth.gr)

Abstract. ~~The main~~One of the main issues arising from the comparison of ground-based and satellite measurements is the difference in spatial representativeness, which for locations with inhomogeneous spatial distribution of pollutants may lead to significant differences between the two datasets. In order to investigate the spatial variability of tropospheric NO_2 within a sub-satellite pixel, a campaign which was lasted for about six months was held at the greater area of Thessaloniki, Greece. Three ~~DOAS/~~MAX-DOAS systems performed measurements of tropospheric NO_2 columns at different sites representative of urban, sub-urban and rural conditions. The direct comparison of these ground-based measurements with corresponding OMI/Aura and GOME-2/MetOp-A and GOME2/MetOp-B products showed good agreement only over the rural area. GOME2A and GOME2B sensors show an average underestimation of tropospheric NO_2 over the urban area of about $10.51\pm8.32 \times 10^{15}$ and $10.21\pm8.87 \times 10^{15}$ molecules cm^{-2}, respectively. The mean difference between ground-based and OMI observations is significantly lower ($8.18\pm7.29 \times 10^{15}$ molecules cm^{-2})~~,~~ ~~mainly due~~ The differences found in the comparisons of MAX-DOAS data with the different satellite sensors can be attributed to the higher spatial resolution of OMI, as well as the different overpass times and NO_2 retrieval algorithms of the satellites. ~~to the higher spatial resolution of OMI~~. OMI data were adjusted using factors calculated by an air quality modelling tool, consisting of the Weather Research and Forecasting (WRF) mesoscale meteorological model and the Comprehensive Air Quality Model with Extensions (CAMx) multi-scale photochemical transport model. This approach resulted to significant improvement of the comparisons over the urban monitoring site. The average difference of OMI observations from Phaethon measurements was reduced to $-4.28\pm6.82 \times 10^{15}$ molecules cm^{-2}.

Keywords: tropospheric NO_2, MAX-DOAS, Phaethon, ground-based, satellite, OMI, GOME-2, air quality modelling, CAMx, Thessaloniki air quality

1 Introduction

Nitrogen oxides (NO_x = NO + NO_2) are among the most important trace components of the atmosphere playing a key role in the tropospheric photochemistry [Seinfeld and Pandis, 1998]. They affect the oxidation capacity and the radiative forcing in the lower atmospheric layers by controlling the ozone formation, contributing to nitric acid (HNO_3) and nitrate radical formation and affecting the hydroxyl levels [Solomon et al., 1999; Finlayson-Pitts and Pitts, 2000]. The main emission sources of nitrogen oxides are fossil-fuels combustion, biomass burning, microbiological processes in the soil, lightning and aircrafts [Lee et al., 1997; Jaeglé et al., 2005]. The most important anthropogenic source is the high-temperature combustion processes occurring in vehicle engines and industrial and power plants [EEA report, 2013]. Hence, urban areas, with heavy road traffic, as well as industrial areas are characterized by inhomogeneous spatial and temporal patterns in NO_x concentrations.

Nitrogen dioxide (NO_2) is mainly produced by the oxidation of nitrogen monoxide (NO) and only a small proportion of NO_x is emitted directly as NO_2 [Hewitt and Jackson, 2009]. However, in the case of diesel vehicles the fraction of directly emitted NO_2 to the total NO_x emissions is much higher, resulting in a significant increase of NO_2 emissions and more frequent breaching of NO_2 air quality limits in urban locations in recent years [Grice et al., 2009; Keuken et al., 2012].

Thessaloniki is the second largest city of Greece with a population of more than 1 million inhabitants about 10% of the total population of the country [Resident Population Census 2011]. The main air pollution sources in Thessaloniki are road transport, domestic heating and industrial facilities, while the air quality of the city is affected by the local topographic and meteorological characteristics and regional pollution transport [Poupkou et al., 2011]. NO_2 concentrations in the city tend to stabilize during the last decades with the highest NO_2 levels observed at the traffic hotspots in the center of the city [Moussiopoulos et al., 2008]. According to Zyrichidou et al. [2009] the mean value of tropospheric NO_2 column until 2008 over Thessaloniki was $3.9\pm3.8 \times 10^{15}$ molecules cm^{-2} and $4.2\pm3.8 \times 10^{15}$ molecules cm^{-2} as observed by GOME-2 and OMI satellite instruments correspondingly.

Well established methods are used worldwide for monitoring NO_2 concentrations based on both in situ measurements from local air quality networks and remote sensing from ground-based instruments and satellite sensors [e.g. Ordonez et al., 2006; Blond et al., 2007; Brinksma et al., 2008]. Space-borne measurements provide information on NO_2 concentrations in a larger scale and over areas, such as oceans and deserts, where ground-based systems cannot be easily deployed. On the other hand, the spatial and temporal resolution of the satellite data ~~is~~ are respectively limited by the satellite footprint size and its overpass time ~~respectively~~. Thus, well-established, extended and relatively dense ground-based networks in areas where significant spatial and temporal variations in NO_2 loading are observed can improve the validation of the satellite data sets.

Remote sensing of NO_2 concentrations is based mainly on the Differential Optical Absorption Spectroscopy (DOAS) analysis [Platt, 1994; Platt and Stutz, 2008] of radiance data, measured either from the space or from the ground. The first studies applying the DOAS method to zenith ground-based measurements for the retrieval of tropospheric and stratospheric NO_2 date back in the ‘70s [Brewer et al., 1973; Noxon et al., 1975]. In the last few decades, the DOAS analysis has been widely applied in ground-based systems for the monitoring of air quality species like NO_2 in the atmosphere and is considered as a reference

technique for the validation of satellite observations [e.g. Celarier et al., 2008; Kramer et al., 2008; Chen et al., 2009; Herman et al., 2009; Irie et al., 2012; Li et al., 2013; Ma et al, 2013; Hendrick et al., 2014]. Several studies have shown that satellite sensors underestimate the tropospheric NO_2 levels over regions characterized by inhomogeneous pollution loadings such as urban and industrial locations. Irie et al. [2012] have shown a clear bias of less than 10% between space-borne and ground-based observations over the Tokyo area in Japan, which is characterized by significant spatial variations in NO_2 concentrations. In Celarier et al. [2008] the correlation coefficient of the comparison of OMI-derived tropospheric NO_2 with different MAX-DOAS instruments at Cabauw, The Netherlands, were found to be about ~0.6. Kramer et al. [2008] estimated similar correlation coefficient between OMI and concurrent MAX-DOAS observations over Leicester, England, while they found significant underestimation of OMI in late-autumn and winter months when comparing with weighted near-surface concentrations. Ma et al. [2013] have shown a systematic underestimation of about 26-38 % in tropospheric NO_2 over Beijing by OMI, depending on the satellite retrieval algorithm and time period.

In this study, tropospheric NO_2 column measurements derived from satellite sensors (OMI/Aura, hereafter OMI, GOME-2/MetOp-A, hereafter GOME2A, and GOME-2/MetOp-B, hereafter GOME2B) are compared with data from MAX-DOAS systems that were deployed in three different sites within the greater area of Thessaloniki, Greece, for a period of a few months. Air quality at these locations, is representative of urban, sub-urban and rural conditions. Adjustment factors calculated by an air quality modelling tool, consisting of the WRF meteorological model and the CAMx air quality model, are applied to ~~satellite~~ OMI data in order to minimize the deviation from ground-based data arising from differences in the spatial representativeness of the two data sets.

2 Observations of NO_2 in the greater Thessaloniki area

2.1 The Phaethon system

Phaethon is a miniature ground-based MAX-DOAS system that performs fast spectrally resolved measurements in the wavelength range 300-450 nm which are used for the retrieval of total and tropospheric columns of atmospheric trace gases. The prototype system was developed in 2006 at the Laboratory of Atmospheric Physics (LAP) in Thessaloniki, Greece [Kouremeti et al., 2008; Kouremeti et al., 2013]. Phaethon has been upgraded recently to improve its performance and two new clone systems have been assembled. The system comprises a cooled miniature CCD spectrograph (AvaSpec-ULS2048LTEC) by Avantes (http://www.avantes.com/), the entrance optics and a 2-axis tracker.

The spectrometer is a symmetrical Czerny-Turner type with 75 mm focal length and a grating of 1800 lines/mm. The slit function has been measured using Cd and Hg spectral lamps and the tunable laser system PLACOS [Nevas et al., 2014] and was found very similar to Gaussian with a full width at half maximum (FWHM) of about 0.25nm for Phaethon #1 and ~0.4 nm for Phaethon #2 and #3. The CCD detector is a Sony 2048-pixel linear array with Deep UV coating that enhances its response below 350 nm and is thermoelectrically cooled to 5°C. The entrance optics comprises a telescope with a planoconvex lens which focusses the collected radiation onto one end of an optical fiber, with a field of view of about 1.5°. Neutral-density

optical filters, cut-off filters and transmission diffuser plates, alone or in various combinations are placed on a filter wheel with 8 positions. One position is clear for scattered radiation measurements and one is opaque for dark-signal measurements. The collected light is transferred through a fused silica UV/Vis optical fiber with high OH and a numerical aperture of 0.22 to the spectrograph entrance slit. The entrance optics is mounted on a 2-axes tracker with pointing resolution of 0.125°, allowing accurate tracking for both direct-sun and sky-radiance measurements at different elevation and azimuth angles. The operating software controls the positioning of the tracker and filter wheel, as well as the data acquisition.

2.2 Ground-based measurements

In the framework of the "Optimization and expansion of ground infrastructure for the validation of satellite-derived column densities of atmospheric species" (AVANTI) project, a short campaign was organized to investigate the spatial variability of tropospheric columns of air pollutants in the greater area of Thessaloniki and the effect of this variability on the comparisons of satellite with ground based data. In addition to the Phaethon system that operates regularly at the roof of the Physics Department in the Aristotle University campus which is located in the center of Thessaloniki with prevailing urban conditions (UC), two identical systems have been deployed at two different locations within an area of about 13 km by 28 km (see Fig. 1). At the exact same locations another campaign has taken place in 2006 to investigate the spatial variability of aerosol optical depth and UV irradiance within an area comparable to the OMI pixel footprint [Kazadzis et al., 2009]. These three locations are characterized by diverse local atmospheric pollution patterns representing urban, suburban and rural conditions. Phaethon #2 was installed at a site with rural conditions (RC) near the sea shore about 28 km south of Thessaloniki city center, where it has been operating from November 1st 2014 through January 31st 2015. Phaethon #3 was installed at the Alexander Technological Educational Institute of Thessaloniki (ATEITH) located in an area with sub-urban conditions (SC) ~13 km north-west of Thessaloniki center and it has been operating there from January 20th to May 11th 2015. Unfortunately, due to a technical problem in one of the spectrometers only a short period of parallel measurements is available at all three locations.

During the campaign the MAX-DOAS systems were performing both direct-sun and scattered light measurements. A sequence of sky radiance measurements included the zenith direction and the off axis elevation angles 2º, 3º, 4º, 5º, 8º, 10º, 12º, 15º, 30º and 45º. ~~These~~ Elevation sequences were performed at azimuth angles of 80º relative to the solar azimuth. Additionally, the same sequence of elevation angles was repeated several times during the day at a fixed azimuth angle of 255º, a direction free of significant obstacles in case of UC site ~~and at azimuth angles of 80º relative to the solar azimuth~~. For this study we used observations at all available azimuth angles, considering that no significant variations with azimuth angle were observed, but only at the elevation angles of 15º and 30º in order to avoid uncertainties introduced due to aerosols ~~loadings~~ at lower elevation angles [Hönninger et al, 2004]. An average of measurements at both elevation angles was calculated if the derived VCDs agreed within 20%, otherwise only data for 30º were compared with satellite retrievals. A similar approach has been applied by Brinksma et al. [2008].

The measured sky radiance spectra were analyzed by means of the QDOAS v2.109_3 software developed by the Royal Belgian Institute for Space Aeronomy (BIRA-IASB) and S[&]T (https://www.stcorp.nl/) [Danckaert et al., 2015]. For the DOAS

analysis the fitting window 400-450 nm was used. A polynomial of order 4, an offset of second order and a Ring effect spectrum, calculated according to the approach described by Chance and Spurr [1997], were also included in the DOAS analysis. Along with the NO_2 cross section at 298K [Vandaele et al., 1998], the cross sections of O_3 at 223K [Bogumil et al., 2003], O_4 at 296K [Greenblatt et al., 1990] and H_2O (HITRAN database, https://www.cfa.harvard.edu/hitran/) were also taken into account. Fig. 2 presents an example of NO_2 slant column fitting for an elevation angle of 5º obtained for the UC site on 6 November 2014, around 10:30 UTC (SZA about 57º). For the retrieval of tropospheric NO_2 the zenith spectrum of each sequence of elevation angles was used as reference in order to minimize the influence of the stratospheric component in the calculated off-axis differential slant column densities (dSCDs) [Hönninger et al, 2004]. The tropospheric vertical column density (VCD) can be calculated for each elevation angle by the formula suggested in Ma et al. [2013]:

$$VCD_{trop} = \frac{dSCD_{trop}}{dAMF_{trop}} \quad (1)$$

where $dAMF_{trop}$ is the tropospheric differential air-mass factor which represents the absorption enhancement in the effective light path caused by the combination of single and multiple scattering and absorption processes.

Look up tables (LUTs) were constructed using radiative transfer simulations to derive the tropospheric NO_2 AMF for each measurement location. These simulations were performed ~~Tropospheric NO_2 AMFs were calculated~~ by means of the modelling package libRadtran version 1.7 [Mayer and Kylling, 2005] using a pseudo-spherical discrete ordinate radiative transfer method [Buras et al, 2011]. ~~For the simulations t~~Typical values of aerosol single scattering albedo (0.95), aerosol asymmetry factor (0.7) and surface albedo (0.1 for UC and 0.07 for the other two sites) were assumed [Bais et al., 2005; Kazantzidis et al., 2006]. A key parameter affecting significantly the radiative transfer simulations and therefore the calculation of AMFs is the trace gas vertical distribution in the atmosphere. In this study, mean vertical profiles were provided by~~from~~ the air quality modelling tool consisting of the photochemical grid model CAMx and the mesoscale weather prediction system WRF ~~were used~~. The description of this modelling tool and details about the simulations are presented in the next section. These vertical profiles decay approximately exponentially with altitude with a scale height of about 0.3 km for UC, 0.65 km for SC and 0.66 km for RC sites. The profiles of SC and RC are comparable, but the NO_2 concentrations in the UC profile are much higher, up to about seven times higher in the lowest atmospheric layer near the surface. For the AMF LUTs ~~simulations~~ the mean vertical profile of the aerosol optical depth (AOD) at 355 nm calculated from observations of the LIDAR system operating in LAP/AUTH during the period 2001-2007 [Giannakaki et al., 2010] was scaled by AOD values in the range 0-1.5. This aerosol information was used for all three locations~~.~~ since, ~~A~~according to Kazadzis et al. [2009], the spatial variability in AOD and its vertical ~~loading and AOD~~ profile ~~between~~ in these ~~three~~ locations is quite small. In that study, t~~T~~he average ~~AOD~~ differences of AOD at 340 nm ~~of~~ at the RC and ~~the~~ SC sites from the UC site were found to be -0.07 and -0.01, respectively, for AOD values ranging between about 0.1 and 1.1, while the long-term (1997-2005) mean AOD over Thessaloniki (UC) is 0.33±0.14 and 0.53±0.17 for winter and summertime, respectively [Kazadzis et al., 2007]. ~~The LIDAR profile was scaled using different total AOD values in the range 0-1.5.~~

~~AMF look-up tables (LUTs) were constructed from the radiative transfer simulations for each measurement location.~~ Along with the AOD, other variables considered for the construction of ~~these~~ LUTs are: the solar zenith angle, the elevation viewing angle and the azimuth angle relative to the solar azimuth. An example of the AMFs calculated at elevation angles 15º and 30º versus AOD for each location is presented in Fig. ~~3~~4. The AMF corresponding to each measurement is calculated by multi-linear interpolation, using AOD measurements from the CIMEL sun-photometer operating at Thessaloniki (http://aeronet.gsfc.nasa.gov/).

Prior to their deployment at the campaign sites, the three systems were operating for a few days in parallel in the University campus and their inter-comparison tests revealed a very good agreement and no systematic differences (Fig. ~~4~~2, Table 2). The hourly mean tropospheric NO_2 measurements performed at both 15˚ and 30˚ elevation angles ~~within 10 minutes~~ were included in the inter-comparison.

2.3 Satellite observations

~~For each of the campaign locations an overpass data set was extracted from OMI, GOME2A and GOME2B observations. Details of this data selection are discussed in Sect. 3.2.~~

The Ozone Monitoring Instrument (OMI) is one of four instruments on board the NASA EOS-Aura spacecraft (http://aura.gsfc.nasa.gov/), launched on 15 July 2004 in a sun-synchronous ascending near-polar orbit with around 1:45 pm local equator crossing time [Levelt et al., 2006]. The OMI detector is a 2-D charge-coupled device (CCD) array. OMI is a compact nadir viewing, wide swath (of 2600 km that permits a near daily global coverage), ultraviolet-visible (270 nm to 500 nm) imaging spectrometer that was contributed to the Aura mission by the Netherlands and Finland. The foot pixel size of OMI at nadir is 13 km × 24 km, degrading towards swath edges (up to 40 km × 160 km at the two ends of the track) [Wenig et al., 2008; ~~[~~Curci et al., 2010]. Beginning in 2007, the so-called "row anomaly" [KNMI, 2012] affected some of the cross-track positions of the swath, reducing the spatial coverage of the instrument. In this work, we use only the unaffected pixels. OMI NO_2 retrievals are obtained from the spectral measurements in the visible spectral range, between 405 and 465 nm. Overpass data of the next-generation version 3 (V3) of the OMI NO_2 standard product (SP), based on the sequential DOAS fitting algorithm [Marchenko et al., 2015], are used in this study. The algorithm used to create NO_2 SP is described by Bucsela et al. [2006; 2013], Wenig et al. [2008] and Celarier et al. [2008]. Marchenko et al. [2015] proposed revisions of the spectral fitting in the OMI NO_2 retrieval algorithm, which reduce the slant column densities by 10–35 %, bringing them closer to independent measurements. The new V3 algorithm also includes improved resolution (1º latitude and 1.25º longitude) a priori NO_2 profiles from Global Modeling Initiative chemistry-transport model with yearly varying emissions. The present version (3.0) uses annual monthly profiles from 2004 to 2014. For dates starting in 2015, the 2014 monthly profiles are used. The use of monthly NO_2 profile shapes captures the seasonal variation in NO_2 profiles [Lamsal et al., 2010]. The a priori profiles' shape presents a close-to-exponential decay with altitude. These profiles are comparable to the mean CAMx profiles that were used as a priori for the SC and RC sites, and, compared to the profile for UC site, they contain much lower NO_2 concentrations in the lowest atmospheric layers [see also section 2.2]. The description and the improvements of the new V3 NO_2 SP are given

in Bucsela et al. [2016] and the references therein in details. The operational total and tropospheric NO_2 columns from OMI are generated by NASA and distributed by the Aura Validation Data Center (AVDC) (http://avdc.gsfc.nasa.gov).

The Global Ozone Monitoring Experiment-2 (GOME-2) instrument is a nadir-viewing scanning spectrometer that samples the 240–790 nm spectral range with a spectral resolution between 0.24–0.5 nm, with an across-track scan time of 6 seconds and a default swath width of 1920 km [Callies et al., 2000]. ~~GOME-2 ground pixels have a footprint size of 80 km x 40 km.~~ Currently there are two GOME-2 instruments operating, one on board EUMETSAT's Meteorological Operational Satellite -A (MetOp-A), launched in October 2006, and the other mounted on the MetOp-B satellite, launched in September 2012. GOME-2 ground pixels have a default footprint size of 80 km x 40 km. Since July 2013, in the tandem mode, GOME2A operates on a reduced swath width of 960 km with an increased spatial resolution (approximately 40 km × 40 km), while GOME2B operates on a nominal wide swath at 1920 km. MetOp-A and MetOp-B are flying on a sun-synchronous orbit with an equator crossing time of 09:30 local time (descending node) and a repeat cycle of 29 days. Global coverage of the sunlit part of the atmosphere can be achieved almost within 1.5 days. From the start of GOME-2 measurements in 2007, the instrument has suffered from sensitivity degradation [Dikty and Richter, 2011; Azam et al., 2015], especially for the wavelengths between 300 and 450 nm (likely due to contamination of optical surfaces). The degradation rates for GOME2B are similar to those for GOME2A (see http://www.eumetsat.int/website/home/TechnicalBulletins/GOME2/index.html). However, the fitting residuals of GOME2B compared to those of GOME2A are much smaller in 2013 and higher in early 2007 [Hao et al., 2014]. According to Hassinen et al. [2016], the impact of GOME-2 instrument degradation on Level-2 product quality depends on the spectral region and the type of retrieval methods selected.

The operational GOME-2 total and tropospheric NO_2 columns from MetOp-A and MetOp-B are generated ~~at~~ by the German Aerospace Center (DLR) using the UPAS (Universal Processor for UV/VIS Atmospheric Spectrometers) environment version 1.3.9, implementing the L~~l~~evel-1-to-2 GOME Data Processor (GDP) version 4.7 algorithm (http://atmos.eoc.dlr.de/gome2/). GDP 4.7 is based on DOAS-style algorithms, originally developed for GOME/ERS-2 [e.g. Spurr et al., 2004]. The data processing is commissioned by EUMETSAT within the auspices of the Satellite Application Facility for Atmospheric composition and UV radiation, O3MSAF, project. The algorithm has two major steps: a DOAS least-squares fitting for the trace gas SCD, followed by the computation of a suitable AMF for the conversion to the VCD. Total NO_2 columns, including a tropospheric and stratospheric component, are retrieved with the DOAS method in the visible wavelength range 425–450 nm [Valks et al., 2011]. In DOAS fitting for optically thin absorbers, such as NO_2 in the visible, the basic model is the Beer-Lambert extinction law. The a priori NO_2 profiles are obtained from a run of the global chemistry transport model (CTM) MOZART version 2 (Horowitz et al., 2003). The profiles can be fitted by an exponential decrease and, similarly to OMI a priori profiles, compare better with RC and SC sites. More details on the GDP 4.7 algorithm can be found in Valks et al. [2011] and Hassinen et al. [2016].

The main features of the two data algorithms are summarized in Table 3. Both satellite data sets show generally good agreement with independent NO_2 measurements [e.g. Valks et al., 2011; Ialongo et al., 2016]. Valks et al. [2011] showed that pollution episodes over the Observatoire de Haute Provence (OHP) were well captured by GOME-2 and the monthly mean tropospheric

columns of MAX-DOAS and GOME-2 are in very good agreement, with differences generally within 0.5×10^{15} molecules/cm^2. In Ialongo et al. [2016] a moderate correlation (r=0.51) was found between the NO_2 total columns' measurements performed by the Pandora spectrometer and the OMI NO_2 V3 in Helsinki 2012. Pandora overestimated the SP V3 and the median relative difference was 32±18%.

For each of the campaign locations an overpass data set was extracted from OMI, GOME2A and GOME2B observations. Details of this data selection are discussed in Sect. 3.2. In Fig. 5 the average tropospheric NO_2 spatial distribution observed by OMI, GOME2A and GOME2B during the campaign period is illustrated. The maps cover a large area around the three campaign stations due to the satellite sensors' coarse spatial resolution. The many white cells, which correspond to lack of sufficiently good quality data, on the OMI map result from OMI sensor's relatively high spatial resolution and row anomalies. The three satellite instruments seem not to clearly detect the high NO_2 concentrations within the planetary boundary layer in the urban area of Thessaloniki, as observed by Phaethon (see also section 3.1) and simulated by the air quality modelling tool (see also section 2.4).

2.4 Air quality modelling tool

The comparison of satellite-derived tropospheric NO_2 with ground-based observations in areas with inhomogeneous distribution of air pollution is usually poor, due to the different geometries associated with the measurement methods of the two datasets [Celarier et al., 2008; Kramer et al., 2008; Irie et al., 2012]. Ground-based measurements are representative of the absorption of radiation in a particular viewing direction and path, while measurements of satellite sensors are sensitive to absorption of radiances emerging from a wide area determined by the size of the satellite pixel. In order to overcome this problem and improve the comparisons in the greater area of Thessaloniki, ~~the satellite~~OMI data are adjusted using factors derived from air quality simulations.

The modeling system employed for the calculation of the adjustment factors consisted of the Comprehensive Air Quality Model with Extensions (CAMx, version 5.3) [ENVIRON, 2010] off-line coupled with the Weather Research and Forecasting - Advanced Research Weather (WRF - ARW, version 3.5.1) [Skamarock et al., 2008]. The model simulations were performed for the period November 2014 – May 2015.

The WRF - ARW is a next-generation mesoscale Numerical Weather Prediction (NWP) model [Kalnay E., 2003] designed to serve both atmospheric research needs and operational weather forecasting. WRF simulations were carried out over two domains in Lambert Conic Conformal projection; a 6 km resolution coarse domain (d01, mesh size of 343 × 273) that covers the greater area of Balkan Peninsula and a nested (two-way nesting) domain (d02) that focuses over the area of Thessaloniki with a higher spatial resolution of 2 km (mesh size of 60 × 60). The domains' vertical profile extends up to 16 km above ground level and contains 28 layers of varying thickness with higher resolution near the ground. The initial and boundary meteorological conditions were taken from the European Centre for Medium – Range Weather Forecast, ECMWF, in spatial resolution of 0.125° × 0.125° (~12.5 km) and temporal resolution of 6 h. Microphysical processes were parameterized using

the New Thompson et al. [2008] scheme, whereas convection in the coarse domain (d01) was parameterized with the Grell-Devenyi (GD) ensemble scheme [Grell and Devenyi, 2002]. For the innermost domain (d02), no convective parameterization was used. Radiative transfer processes were handled with the shortwave and longwave RRTMG schemes [Iacono et al., 2008]. The surface layer was parameterized using the Eta similarity scheme [Janjic, 2002], while for the planetary boundary layer the Mellor-Yamada-Janjic parameterization scheme [Janjic and Zavisa, 1994] was used. Finally, for the parameterization of land surface processes the Noah Land Surface Model [Tewari, et al., 2004] was applied.

CAMx is a 3D Eulerian photochemical dispersion model widely used in air quality studies during the last decade [Liora et al., 2016; Poukou et al., 2014; Kukkonen et al., 2012; Lee et al., 2009; Lei et al., 2007] several of which are related to joint analysis of simulated and remotely sensed pollutant concentration data [Zyrichidou et al 2009; 2013; 2015; Zyryanov et al 2012; Huijnen et al 2010]. In the current study, the simulation domains of CAMx were identical, in terms of horizontal spatial resolution and projection, with those of the WRF model in order to avoid errors introduced by interpolations between grids, but were slightly less spatially extended (337 x 267 cells for the Balkan domain and 56 × 56 cells for the Thessaloniki domain). CAMx grids were structured in 22 vertical layers extending up to 10 km above ground level. The gaseous and particulate matter anthropogenic emissions for the Balkan domain were derived from the European scale emission database of The Netherlands Organisation (TNO) for the reference year 2007 [Kuenen et al., 2011]. For the greater area of Thessaloniki, the anthropogenic emissions were calculated using mainly the methodologies and emission factors of the EMEP/CORINAIR emission inventory guidebook [EEA, 2006]. More specifically, the anthropogenic emission model MOSESS (Model for the Spatial and Temporal Distribution of Emissions) [Markakis et al., 2013] was applied for the calculation of CO, NOx, SO_2, NH_3, NMVOC, PM10 and PM2.5 emissions as well as for their chemical, spatial and temporal analysis. The total NOx emissions for the domain of Thessaloniki ~~during the period of the campaign~~for the months November to May are presented in the upper panel of Fig. ~~6~~5~~5~~. The monthly NOx emissions pattern for each of the months November to May is similar to that presented in Fig. 6 characterized by higher emission density over the urban center due to enhanced anthropogenic activities (mostly road transport). Particulate matter emissions from natural sources (windblown dust, sea salt) as well as biogenic volatile organic compounds from vegetation were estimated using the Natural Emissions model (NEMO) [Poupkou et al., 2010; Liora et al., 2015; Liora et al., 2016]. The gas-phase chemical mechanism employed in CAMx was the 2005 version of Carbon Bond (CB05) [Yarwood et al., 2005]. The chemical boundary conditions for CAMx runs were taken from the global model system C-IFS-TM5 results, available in the framework of the EU project MACC-III.

The adjustment factors of ~~the satellite~~OMI data were calculated by the following procedure: For each 2 km × 2 km grid cell included in a typical OMI pixel size area at nadir (7 × 13 cells), centered at the location of each monitoring site, the tropospheric NO_2 VCD was derived by integrating vertically the model-derived hourly mean mixing ratios of NO_2. The lower panel in Fig. ~~6~~5~~5~~ presents the simulated NO_2 VCD averaged over the period of the campaign for each cell of the simulations domain. The tropospheric NO_2 follows the NOx emissions pattern. ~~within the OMI footprint over the three campaign sites~~. Then ~~t~~he tropospheric NO_2 VCD for the grid cell that contains the coordinates of each monitoring site was divided by the VCD averaged over the OMI pixel area. Finally, the OMI data were multiplied by these adjustment factors in order to minimize the effect of

the differences in the spatial distribution of NO_2 and achieve better agreement with the ground-based observations, which are assumed to represent mostly the VCD above the grid cell where they are located.

It should be mentioned here that the method was applied only to OMI data because for GOME-2 the satellite pixel is very large, covering typically the entire domain of Fig. 1. A similar method has been previously employed on comparisons of GOME2A tropospheric NO_2 observations with ground-based data over the Observatoire de Haute Provence (OHP) at southern France [Lambert et al., 2011], leading to a slight improvement of the correlation coefficient from 0.63 to 0.71 and the slope of the linear regression from 0.69 to 0.73.

It should be also noted that, based on calculations of the representativeness area of the MAX-DOAS measurements presented in this study, the 2x2 km^2 model cell used for the adjustment factors calculation can be considered representative of the measurement light path. For MAX-DOAS observations near the surface under high aerosol conditions an approach based on O_4 retrieval should be used for the estimation of the horizontal representativeness area [Wagner et al., 2004; Richter et al., 2013]. However, the effect of the aerosol loading and, thus, the atmospheric visibility for observations at the elevation angles of 15˚ and 30˚ can be considered relatively weak. Moreover, the horizontal distance, of which these measurements are representative, is quite small, especially for an absorber layer located near the surface. Hence, the horizontal sensitivity range was estimated for the campaign period and OMI overpass time using the elevation viewing angle and boundary layer height (BLH) reanalysis data from ECMWF, as the ratio of the BLH to the tangent of the elevation angle (Thomas Wagner, personal communication). By this method, an average value of 0.55 km was obtained. During spring months the representativeness area can be up to about 10 km. However, only for about 2% of the campaign measurements the horizontal distance is larger than 2 km, because the majority of the measurements were performed from late-autumn through early-spring, when the BLH is shallower. Irie et al. [2011] estimated a horizontal sensitivity distance of roughly 10 km for MAX-DOAS measurements performed at Cabauw, the Netherlands during the period from 8 June to 24 July 2009 using a geometrical approach based on box-AMFs.

3 Results and discussion

3.1 NO_2 tropospheric columns in the greater area of Thessaloniki

The hourly mean tropospheric NO_2 measurements obtained by Phaethon at the three campaign sites are presented in Fig. 7~~6~~. The NO_2 at the city center of Thessaloniki (UC) in blue circles are much higher than at the SC (red circles) and RC (yellow circles) sites, especially during winter months. The NO_2 levels observed in the urban area during spring months are slightly lower compared to those in the winter considering also the small temporal variability of monthly road transport emissions, representing the major emission source in the urban center. The averaged measured tropospheric NO_2 over the campaign period is ~$12.32 \pm 7.46 \times 10^{15}$ molecules cm^{-2} for the center of Thessaloniki, whereas the mean values for the SC and RC sites are $5.94 \pm 3.58 \times 10^{15}$ and $4.79 \pm 2.36 \times 10^{15}$ molecules cm^{-2}, respectively. The average tropospheric NO_2 at SC and RC sites are in general comparable. However, some positive excursions are observed at SC because this site is likely affected by NO_2

transported from urban areas or by local pollution sources depending on weather conditions. The SC site is adjacent to the city center and to Thessaloniki's industrial area, although industrial activity has been drastically reduced over the last five years. Negative values of the VCD obtained from measurements at higher elevation angles, such those used in this study (15˚ and 30˚ as discussed in section 2.2), indicate that the NO_2 absorption of the Fraunhofer reference spectrum is underestimated and cannot be assumed negligible compared to the analyzed spectra.

3.2 Comparison of ground-based tropospheric NO_2 with OMI, GOME-2/MetOp-A and GOME-2/MetOp-B observations

For each of the three campaign sites ground-based measurements of tropospheric NO_2 (both 15º and 30º were used as described in section 2.2) are compared with products from satellite overpass data. The collocation criteria used are the solar zenith angle (SZA), the cloud fraction (CLF) and the temporal and spatial difference of the measurements. More specifically, only satellite data corresponding to SZA ≤ 75º and CLF ≤ 20% (corresponds to observations with a radiance reflectance of less than 50% from clouds [van der A et al., 2008]) were selected and averages of Phaethon measurements within ±30 min around the overpass time were included in the comparison. Moreover, only OMI pixels that are not affected by the OMI row anomalies [see OMI Data User's Guide, 2012] were used in this study in order to obtain good quality and meaningful data. Finally, the upper limit for the distance between the measurement site and the center of the sub-satellite pixel was set to 25 km for OMI and 50 km for GOME-2 sensors, in correspondence to their typical pixel sizes. In order to improve the possibility that the station is located within the pixel area, the closest OMI pixel was selected for the comparisons, whereas in the case of GOME-2 sensors the average measurement of all pixels within the distance limit of 50 km was calculated. However, the comparison results seem not to be significantly affected when the 50 km limit is used for both OMI and GOME-2 sensors, or when the closest GOME-2 pixel is chosen instead of the average value.

Scatter plots of tropospheric NO_2 data for each campaign site and satellite sensor separately are presented in Fig. 8~~7~~, while averages and statistics of the comparisons are shown respectively in Tables 4 and 5. The satellite instruments seem to underestimate significantly the NO_2 levels over the urban area of Thessaloniki (right column in Fig. 8~~7~~, Table 4 and Table 5). This finding might be ascribed to the fact that the satellite-derived columns represent the average pollution loading in the sub-satellite pixel area, while ground-based data are mostly representative of the NO_2 amounts in air masses above and in close proximity to the monitoring site. In the case of Thessaloniki, the significant contribution of lower pollution levels in the suburbs results into lower estimates of NO_2 by the satellite. Several studies have reported significant differences in air pollution between the city center and the suburbs using long-term observations by the air quality monitoring network of Central Macedonia [Poupkou et al., 2011; Moussiopoulos et al., 2008].

The statistics calculated from the comparison between the ground-based and OMI measurements over the UC and SC stations (Table 5) are similar to those found in previous studies. For example, the correlation coefficients estimated by Kramer et al. [2008] and Celarier et al. [2008] at Leicester, England and Cabauw, The Netherlands, respectively, are about 0.6. In Ialongo et al. [2016] linear fit slopes of 0.49 and 0.39 for V2.1 and V3 OMI retrieval algorithms, respectively, and r = 0.51 for both

were found when compared with Pandora observations in Helsinki. Similarly, OMI measurements at NASA Goddard Space Flight Center were ~25% lower than the Brewer data with an r value of 0.58 in daily values, a slope of 0.75 (±0.14) and an intercept of -0.38 (±2.5) × 10^{15} molecules/cm^2 [Wenig et al., 2008].

The fact that OMI observations compare better with the ground-based NO_2 data can be attributed mainly to ~~its smaller~~the different satellite pixel sizes ~~-~~and to ~~its~~ OMI's high~~er~~ sensitivity in the boundary layer [e.g. Wallace et al., 2009]. ~~compared to GOME-2.~~ The OMI sensor provides better detection of higher local pollution levels [Kramer et al., 2008], due to its higher spatial resolution (13 × 24 km^2 at nadir), compared to GOME-2 sensors which detect the average NO_2 concentration over a larger area (40 × 40 km^2 for MetOpA and 80 × 40 km^2 for MetOpB). Moreover, the differences observed between the OMI and GOME-2 data sets as well as in the comparison with the MAX-DOAS data can be explained by the difference in satellite overpass time. OMI passes over Thessaloniki at around local solar noon (~10:30 UT), when tropospheric NO_2 levels are normally reduced due to photochemical processes [Crutzen, 1979]. On the contrary, GOME2A and GOME2B pass over Thessaloniki during morning hours (between 7:30 - 9:00 UT), when local NO_2 concentrations in the city center are usually much higher. The different algorithms used for the retrieval of tropospheric NO_2 from OMI and GOME-2 measurements, and mainly the different spectral ranges used in the DOAS analysis and different a priori profiles (Table 3), also play an important role.

The r values calculated for GOME2A and GOME2B over UC site are 0.28 and 0.19 respectively. Better correlation coefficient and slope values, 0.51 and 1.2 (±0.049) respectively, between daily averaged MAX-DOAS and GOME2A tropospheric NO_2 columns were found by Valks et al. [2011], showing that pollution episodes over the Observatoire de Haute Provence (OHP) were well captured by GOME-2. Ground-based and satellite-derived NO_2 tropospheric VCDs are in better agreement over the rural (RC) and sub-urban (SC) stations (left and middle columns respectively in Fig. 8~~7~~, Table 4 and Table 5). However, there is poor correlation between Phaethon and GOME-2 sensors over those two locations (Table 5) probably due to the limited number of data pairs and some elevated NO_2 concentrations observed by the Phaethon system over the SC location which are not detected by GOME-2 sensors.

Differences observed between GOME2A and GOME2B results (Fig. 8, Tables 4 and 5) could be attributed mainly to their different pixel sizes, as GOME2B footprint has double the size of GOME2A, and partly to their different instrumental degradation, considering that the same retrieval algorithm is used. In general, the slope, intercept and r values from the comparison between GOME2A and MAX-DOAS are better than in case of GOME2B (Table 5). However, the mean bias of GOME2A from the ground-based data is about half compared to the GOME2B bias over the RC site but slightly higher over the SC and UC sites. Interestingly, the difference between GOME2A and GOME2B mean values (Table 4) is larger for the RC site and smaller for the SC and UC areas, which is not consistent with the pixel size influence. Especially in case of UC site a better detection of the higher NO_2 loadings in the city center by GOME2A should be expected, which, as can be seen also from the mean satellite NO_2 columns in Fig.5, is not the case.

3.3 Reconstruction of OMI observations

Hourly data of tropospheric NO_2 derived from the CAMx simulations according to the method described in section 2.4 are presented for each campaign location separately in Fig. 98 (left panels), averaged over the OMI nadir pixel and for the grid point of 2×2 km^2 corresponding to the location of each ground-based ~~site~~instrument. Adjustment factors, i.e. ratios of these simulations, are also shown in Fig. 97 (right panels, grey lines) for all hourly data in each day. As expected, the adjustment factor is variable during each day with increasing variability from the RC to the UC sites. Adjustment factors corresponding to the OMI overpass time, which were used for the reconstruction of the satellite dataset, are presented with colored lines. For the center of Thessaloniki (UC) the mean estimated ratio is 2.20 ± 0.75 (right column in Table 6). Relatively higher values are observed during spring (2.39 ± 0.80) and smaller during the winter months (2.03 ± 0.64). At the other two locations the adjustment ratio is much smaller. In the case of the RC site (left column in Table 6), the ratio is on average close to unit (0.96 ± 0.18). This indicates that the area within the OMI nadir pixel size corresponds mostly to lower NO_2 levels, same as the Phaethon monitoring site. On the other hand, the majority of the ratios calculated for the SC location (middle row in Fig. 97) are slightly lower than 1, leading to an average of 0.78 ± 0.24, which indicates higher average NO_2 concentrations over the OMI footprint than at the ground-based monitoring site. These results can be ascribed to the fact that the SC station is located about 13 km west of the center of Thessaloniki, hence, the sub-satellite pixel area can be affected by heavy pollution levels observed in the city center. However, ratios larger than unit are observed occasionally (~11% of all simulations), possibly related to local pollution sources or to NO_2 transportation by the prevailing winds from neighboring locations.

The horizontal representativeness of the light path used in the MAX-DOAS analysis is well within the 2×2 km^2 model cell (see also section 2.4). In order to investigate the effect on the adjustment factors, we repeated the calculations using two or three CAMx cells in the light path direction. The difference in the resulted mean factors (Table 6), when two cells are used, is about 1-2% in all cases except for the UC site during the OMI overpass time (difference of ~5%). When the averages of three cells are used in the calculations, the absolute differences are in general higher, e.g up to about 5% in the SC site and 13% in the UC site. The much higher decrease in the UC site can be explained by the influence in some light path directions of the lower NO_2 concentration levels over the sea which is very close to the urban area (Fig. 6). It is worth mentioning that in the RC site the average ratio when all simulations are considered is around unity despite the number of cells taken into account. In all other cases, except in the UC site when all simulations are considered, the differences in the resulted ratios using more than one cells are negative, which means that the average tropospheric NO_2 is lower when the light path is extended further away from the measurement location.

The comparison between ground-based and OMI observations over the campaign locations before and after the satellite data adjustment is presented in Fig. 109. Over the UC monitoring site Phaethon compares better with the adjusted OMI data. The OMI average underestimation has changed from 8.18±7.29 × 10^{15} to 4.28±6.82 × 10^{15} molecules cm^{-2} and the slope of the fitted least squares regression line has been improved from ~0.2 to ~0.4. The OMI data over the other two campaign stations have not been significantly affected by the adjustment, due to better spatial homogeneity of the NO_2 loading. It should be

noted here that the calculation of the adjustment factors assumed that the OMI pixel is centered at the monitoring site and its size is always equal to the typical nadir pixel. In reality, these assumptions are not always valid [de Graaf et al., 2016], therefore the method of deriving adjustment factors is associated with some uncertainty which increases with pixel size and distance of its center from the ground-based monitoring system. The use of actual satellite geometry for each day is complex and would require a much larger domain for the air-quality simulations, more than double the currently used (120×120 km^2) in order to include all possible pixel sizes and positions for each location. However, such simulations were not available for this study.

Additional uncertainties may arise from the vertical integration of the air-quality simulations to derive vertical column of NO_2 representative for the troposphere and the assumption that it is comparable to the VCD derived by the MAX-DOAS measurements. The two methods are based on different concepts, and for the MAX-DOAS it is not possible to define a top level for the tropospheric NO_2 column which could be used to integrate vertically the model simulations. The importance of this effect was investigated in a sensitivity analysis which showed that the uncertainty in the calculation of the VCD of NO_2 associated with the upper level used in the vertical integration of the model derived mixing ratio is less than 1% for different upper levels between 6 and 9 km.

4 Summary and conclusions

An experimental campaign took place in the greater Thessaloniki area, Greece, within the period November 2014 – May 2015, with the aim to investigate the impact of different spatial sampling of ground-based and space borne measurements on tropospheric NO_2 column density. In this study, tropospheric NO_2 derived by the Phaethon ground-based ~~DOAS/~~MAX-DOAS systems at three different locations characterized by diverse pollution loadings were presented and compared with corresponding satellite products of OMI/Aura and GOME-2/MetOp-A and /MetOp-B. The agreement of Phaethon measurements with satellite columns over the rural area is good for all three instruments, although the variability is higher for GOME2B. A strong positive bias in ground-based NO_2 columns is found over the urban area. This is attributed to the great inhomogeneity of NO_2 concentrations over the area covered by the city of Thessaloniki. A significant portion of the area surrounding the city center and included in a typical sub-satellite pixel corresponds mostly to rural atmospheric conditions. Therefore the average tropospheric NO_2 is significantly reduced compared to Phaethon data that probe air masses over the urban center of the city.

The agreement of Phaethon data with OMI retrievals is better compared to GOME-2 sensors, due mainly to its smaller pixel footprint. For GOME2A and GOME2B the city center is a very small portion compared to the entire area covered by the satellite pixel, thus the contribution of the increased NO_2 loadings to the average column density is very weak. The differences between the two satellite retrieval algorithms as well as the different overpass times also play an important role. Differences observed between GOME2A and GOME2B tropospheric NO2 can be explained by their different pixel sizes and instrumental degradation. Our findings from the comparison between MAX-DOAS and OMI overpass data agree with the results of previous

validation studies [e.g. Kramer et al., 2008; Ialongo et al., 2016]. However, we have calculated smaller correlation coefficients between the MAX-DOAS and GOME-2 data compared to other studies [e.g. Valks et al., 2011].

The application of adjustment factors ~~on OMI data~~ derived from NO_2 simulations with an air quality modelling tool on OMI data reduced the effect of spatial differences between OMI and Phaethon observations. The improvement in the comparisons is more evident for the urban site, where the mean difference between OMI and Phaethon were reduced from -8.18±7.29 × 10^{15} to -4.28±6.82 × 10^{15} molecules cm^{-2}. The effect on the rural and suburban locations is negligible, due to the reduced spatial inhomogeneity of the air-pollution.

Acknowledgements: This study was conducted in the framework of the QA4ECV (Quality Assurance for Essential Climate Variables) project, that was financed under theme 9 (Space) of the European Union Framework Program 7. The three Phaethon systems have been developed in the framework of the Operational Program "Education and Lifelong Learning" of the National Strategic Reference Framework (NSRF) Research Funding Program: ARISTEIA I - 608, AVANTI (Optimization and expansion of ground infrastructure for the validation of satellite-derived column densities of atmospheric species) project, that was co-financed by the European Union (European Social Fund-ESF) and Greek national funds. The authors would like to thank the Earth Observation Center, Remote Sensing Technology Institute, German Remote Sensing Data Center, DLR, for the dissemination of the GOME2/MetopA data and the NASA Earth Science Division for funding the OMI NO_2 development. C-IFS-TM5 global model system data were provided in the framework of the EU project Monitoring Atmospheric Composition and Climate III (MACC-III) (Grant agreement no: 633080). Finally, we would like to thank TNO for the European scale anthropogenic emission data provided in the framework of the EU project Monitoring Atmospheric Composition and Climate (MACC) (Grant agreement no.: 218793).

References

Acarreta, J. R., J. F. deHaan, and P. Stammes , Cloud pressure retrieval using the O2-O2 absorption band at 477 nm, J. Geophys. Res., 109, D05204, doi:10.1029/2003JD003915, 2004.

Azam, F., A. Richter, M. Weber, S. Noël and J. P Burrows, GOME-2 on MetOp-B Follow-on analysis of GOME2 in orbit degradation, EUM/CO/09/4600000696/RM, Final Report, 2015.

Bais, A. F., A. Kazantzidis, S. Kazadzis, D. S. Balis, C. S. Zerefos, and C. Meleti, Deriving an effective aerosol single scattering albedo from spectral surface UV irradiance measurements, Atmospheric Environment, 39(6), 1093-1102, doi: http://dx.doi.org/ 10.1016/j.atmosenv.2004.09.080, 2005.

Blond, N., et al., Intercomparison of SCIAMACHY nitrogen dioxide observations, in situ measurements and air quality modelling results over western Europe. J. Geophys. Res. 112, D10311. http://dx.doi.org/ 10.1029/2006JD007277, 2007.

Bogumil K., J. Orphal, T. Homann, S. Voigt, P. Spietz, O.C. Fleischmann, A. Vogel, M. Hartmann, H., Bovensmann, J. Frerick, and J.P. Burrows, "Measurements of molecular absorption spectra with the SCIAMACHY pre-flight model:

Instrument characterization and reference data for atmospheric remote sensing in the 230-2380 nm region," J. Photochem. Photobiol. A: Chem. 157, 167-184, 2003.

Brewer, A.W., McElroy, C.T., Kerr, J.B. Nitrogen dioxide concentration in the atmosphere. Nature 1973, 246, 129–133.

Brinksma, E.J., Pinardi, G., Volten, H., Braak, R., Richter, A., Schonhardt, A. et al., The 2005 and 2006 DANDELIONS NO2 and aerosol intercomparison campaigns. J. Geophys. Res. 113, D16S46, 2008.

Buras R., Dowling T., and Emde C., New secondary-scattering correction in DISORT with increased efficiency for forward scattering. Journal of Quantitative Spectroscopy & Radiative Transfer, v. 112, iss. 12, p. 2028-2034, 2011.

Bucsela, E. J., Celarier, E. A., Wenig, M. O., Gleason, J. F., Veefkind, J. P., Boersma, K. F., and Brinksma, E. J.: Algorithm for NO_2 vertical column retrieval from the Ozone Monitoring Instrument, IEEE Trans. Geosci. Remote Sens., 44, 1245–1258, 2006.

Bucsela, E. J., Krotkov, N. A., Celarier, E. A., Lamsal, L. N., Swartz, W. H., Bhartia, P. K., Boersma, K. F., Veefkind, J. P., Gleason, J. F., and Pickering, K. E.: A new stratospheric and tropospheric NO_2 retrieval algorithm for nadir-viewing satellite instruments: applications to OMI, Atmos. Meas. Tech., 6, 2607– 2626, doi:10.5194/amt-6-2607-2013, 2013.

Bucsela Eric J., Edward A. Celarier, James L. Gleason, Nickolay Krotkov, Lok N. Lamsal, Sergey V. Marchenko, William H. Swartz, OMNO2 README Document Data Product Version 3.0, Document version 7.0, September 2016.

Callies, J., E. Corpaccioli, M. Eisinger, A. Hahne, and A. Lefebvre, GOME-2: Metop's second generation sensor for operational ozone monitoring, ESA Bull., 102, 28–36, 2000.

Celarier, E. A., et al., Validation of Ozone Monitoring Instrument nitrogen dioxide columns, J. Geophys. Res., 113, D15S15, doi:10.1029/2007JD008908, 2008.

Chance, K., Spurr, R.J.D. Ring effect studies: Rayleigh scattering, including molecular parameters for rotational Raman scattering and the Fraunhofer spectrum. Appl. Opt. 36, 5224–5230, 1997.

Chen, D., Zhou, B., Beirle, S., Chen, L. M., and Wagner, T.: Tropospheric NO2 column densities deduced from zenith-sky DOAS measurements in Shanghai, China, and their application to satellite validation, Atmos. Chem. Phys., 9, 3641–3662, doi:10.5194/acp-9-3641-2009, 2009.

Crutzen, P. J., The role of NO and NO_2 in the chemistry of the troposphere and stratosphere, In: Annual review of earth and planetary sciences. Volume 7. (A79-37176 15-42) Palo Alto, Calif., Annual Reviews, Inc., p. 443-472., 1979.

Curci, G., Palmer, P. I., Kurosu, T. P., Chance, K., and Visconti, G.: Estimating European volatile organic compound emissions using satellite observations of formaldehyde from the Ozone Monitoring Instrument, Atmos. Chem. Phys., 10, 11501-11517, doi:10.5194/acp-10-11501-2010, 2010.

Danckaert, T., Fayt, C., Van Roozendael, M., et al.: QDOAS software user manual 2.109, IASB/BIRA, Uccle, Belgium, 2015.

de Graaf, M., Sihler, H., Tilstra, L. G., and Stammes, P.: How big is an OMI pixel?, Atmos. Meas. Tech. Discuss., doi:10.5194/amt-2016-61, in review, 2016.

Dikty, S. and Richter, A.: GOME-2 on MetOp-A Support for Analysis of GOME-2 In-Orbit Degradation and Impacts on Level 2 Data Products, Final Report, Version 1.2, 14 October 2011.

Douglass A. R., Stolarski, R. S., Strahan, S. E., and Connell, P. S.: Radicals and reservoirs in the GMI chemistry and transport model: Comparison to measurements, J. Geophys. Res., 109, D16302, doi:10.1029/2004JD004632, 2004.

Drosoglou T., A. F. Bais, I. Zyrichidou, A. Poupkou, N. Liora, C. Giannaros, M. E. Koukouli, N. Kouremeti, S. Dimopoulos, D. Balis, D. Melas.: Comparison of Ground-Based Tropospheric NO2 Columns with OMI/Aura Products in the Greater Area of Thessaloniki by Means of an Air Quality Modeling Tool, Perspectives on Atmospheric Sciences, Springer Atmospheric Sciences, e-book of proceedings, Online ISBN: 978-3-319-35095-0, DOI 10.1007/978-3-319-35095-0_153, Part III, Pαges pp 1075-1080, 2016.

EEA, 2006. EMEP/CORINAIR Emission Inventory Guidebook 2006. European Environment Agency Technical Report no.30. Available at http://www.eea.europa.eu/publications/EMEPCORINAIR4

EEA, 2013. Air Quality in Europe – 2013 report. European Environment Agency Report No 9. Available at http://www.eea.europa.eu/publications/air-quality-in-europe-2013.

ENVIRON, 2010. User's guide CAMx - Comprehensive Air Quality Model with extensions, Version 5.30, ENVIRON International Corporation, 415.899.0700, December 2010.

Finlayson-Pitts, B. S., Barbara J., and Pitts Jr., J. N.: Chemistry of the Upper and Lower Atmosphere, J. Atmos. Chem., 39, 327–332, doi: 0.1023/A:1010697311969, 2001.

Giannakaki, E., Balis, D. S., Amiridis, V., and Zerefos, C.: Optical properties of different aero-sol types: seven years of combined Raman-elastic backscatter lidar measurements in Thessaloniki, Greece, Atmos. Meas. Tech., 3, 569-578, doi:10.5194/amt-3-569-2010, 2010.

Greenblatt G.D., J.J. Orlando, J.B. Burkholder, and A.R. Ravishankara, "Absorption measurements of oxygen between 330 and 1140 nm," J. Geophys. Res. 95, 18577-18582, 1990.

Grell G.A., Devenyi D., A generalized approach to parameterizing convection combining ensemble and data assimilation techniques. *Geophys. Res. Lett.*, 29(14), 2002.

Grice, S., Stedman, J., Kent, A., Hobson, M., Norris, J., Abbott, J., Cooke, S., Atmospheric Environment, (43/13), 2 154–2 167, 2009.

Hao, N., Koukouli, M. E., Inness, A., Valks, P., Loyola, D. G., Zimmer, W., Balis, D. S., Zyrichidou, I., Van Roozendael, M., Lerot, C., and Spurr, R. J. D.: GOME-2 total ozone columns from MetOp-A/MetOp-B and assimilation in the MACC system, Atmos. Meas. Tech., 7, 2937–2951, doi:10.5194/amt-7-2937-2014, 2014.

Hassinen, S., et al., Overview of the O3M SAF GOME-2 operational atmospheric composition and UV radiation data products and data availability, Atmos. Meas. Tech., 9, 383-407, doi:10.5194/amt-9-383-2016, 2016.

Hendrick, F., Müller, J.-F., Clémer, K., Wang, P., De Mazière, M., Fayt, C., Gielen, C., Hermans, C., Ma, J. Z., Pinardi, G., Stavrakou, T., Vlemmix, T., and Van Roozendael, M.: Four years of ground-based MAX-DOAS observations of HONO and NO2 in the Beijing area, Atmos. Chem. Phys., 14, 765-781, doi:10.5194/acp-14-765-2014, 2014.

Herman, J., A. Cede, E. Spinei, G. Mount, M. Tzortziou, and N. Abuhassan, NO2 column amounts from groundbased Pandora and MFDOAS spectrometers using the direct-sun DOAS technique: Intercomparisons and application to OMI validation, J. Geophys. Res., 114, D13307, doi:10.1029/2009JD011848, 2009.

Hewitt C.N. and Jackson A.V.: Atmospheric Science for Environmental Scientists, Wiley-Blackwell, 2009.

Hönninger, G., von Friedeburg, C., and Platt, U.: Multi axis differential optical absorption spectroscopy (MAX-DOAS), Atmos. Chem. Phys., 4, 231-254, doi:10.5194/acp-4-231-2004, 2004.

Horowitz, L., Walters, S., Mauzerall, D., Emmons, L., Rasch, P., Granier, C., Tie, X., Lamarque, J., Schultz, M., Tyndall, G., Orlando, J., and Brasseur, G., A global simulation of tropospheric ozone and related tracers: description and evaluation of MOZART, version 2, J. Geophys. Res., 108(D24), 4784, doi:10.1029/2002JD002853, 2003.

Huijnen, V., Eskes, H., Poupkou, A., Elbern, H., Boersma, K. F., Foret, G., Sofiev, M., Valdebenito, A., Flemming, J., Stein, O., Gross, A., Robertson, L., D'Isidoro, M., Kioutsioukis, I., Friese, E., Amstrup, B., Bergstrom, R., Strunk, A., Vira, J., Zyryanov, D., Maurizi, A., Melas, D., Peuch, V.-H. and Zerefos, C., "Comparison of OMI NO2 tropospheric columns with an ensemble of global and European regional air quality models", Atmospheric Chemistry and Physics, 10, pp. 3273–3296, 2010.

Iacono M.J., Delamere J.S., Mlawer E.J., Shephard M.W., Clough S.A., Collins W.D., Radiative forcing by long–lived greenhouse gases: Calculations with the AER radiative transfer models. J. Geophys. Res., 113, D13103, 2008.

Ialongo I., J. Herman, N. Krotkov, L. Lamsal, et al., Comparison of OMI NO2 observations and their seasonal and weekly cycles with ground-based measurements in Helsinki, Atmos. Meas. Tech., 9, 5203–5212, 2016.

Irie, H., Takashima, H., Kanaya, Y., Boersma, K. F., Gast, L., Wittrock, F., Brunner, D., Zhou, Y. and Van Roozendael, M.: Eight-component retrievals from ground-based MAX-DOAS observations, Atmos. Meas. Tech., 4(1), 1027–1044, doi:10.5194/amtd-4-639-2011, 2011.

Irie, H., Boersma, K. F., Kanaya, Y., Takashima, H., Pan, X., and Wang, Z. F.: Quantitative bias estimates for tropospheric NO2 columns retrieved from SCIAMACHY, OMI, and GOME-2 using a common standard for East Asia, Atmos. Meas. Tech., 5, 2403-2411, doi:10.5194/amt-5-2403-2012, 2012.

Jaeglé, L., Steinberger, L., Martin, R.V., Chance, K., Global partitioning of NOx sources using satellite observations: relative roles of fossil fuel combustion, biomass burning and soil emissions. Faraday Discuss. 130, 407–423. http://dx.doi.org/10.1039/b502128, 2005.

Janjic Z.I., Zavisa I., The Step–Mountain Eta Coordinate Model: Further developments of the convection, viscous sublayer, and turbulence closure schemes. *Mon. Wea. Rev.*, **122**, 927–945, 1994.

Janjic Z.I., Nonsingular implementation of the Mellor-Yamada Level 2.5 Scheme in the NCEP Meso model. *NCEP Office Note No. 437*, 61 pp, 2002.

Kalnay, E.: Atmospheric Modeling, Data Assimilation, and Predictability. Cambridge University Press, 341 pp., 2003.

Kazadzis, S., Bais, A., Amiridis, V., Balis, D., Meleti, C., Kouremeti, N., Zerefos, C. S., Rapsomanikis, S., Petrakakis, M., Kelesis, A., Tzoumaka, P., and Kelektsoglou, K.: Nine years of UV aerosol optical depth measurements at Thessaloniki, Greece, Atmos. Chem. Phys., 7, 2091-2101, doi:10.5194/acp-7-2091-2007, 2007.

Kazadzis, S., Bais, A., Balis, D., Kouremeti, N., Zempila, M., Arola, A., Giannakaki, E., Amiridis, V., and Kazantzidis, A.: Spatial and temporal UV irradiance and aerosol variability within the area of an OMI satellite pixel, Atmos. Chem. Phys., 9, 4593-4601, doi:10.5194/acp-9-4593-2009, 2009.

Kazantzidis, A., A. Bais, K. Garane, S. Kazadzis, and C. Meleti, Estimation of UV irradiance from ancillary data and comparison with measurements at Thessaloniki, Greece (40.5°N, 23°E), SPIE Proceedings Vol. 6362: Remote Sensing of Clouds and the Atmosphere XI, doi:10.1117/12.689813, 2006.

Keuken M. P., Roemer M. G. M., Zandveld P., Verbeek R. P., Velders G. J. M., Trends in primary NO2 and exhaust PM emissions from road traffic for the period 2000 e 2020 and implications for air quality and health in the Netherlands Trends in primary NO_2 and exhaust PM emissions from road traffic for the period 2000–2020 and implications for air quality and health in the Netherlands, Atmos. Environ., vol. 54, pp. 313-319, 2012.

KNMI: Background information about the Row Anomaly in OMI, available at: http://www.knmi.nl/omi/research/product/rowanomaly-background.php, 2012.

Kouremeti N, Bais A.F., Kazadzis S, Blumthaler M., and Schmitt R., "Charge-coupled device spectrograph for direct solar irradiance and sky radiance measurements," Appl. Opt. 47, 1594-1607, 2008.

Kouremeti, N., Bais, A. F., Balis, D., and Zyrichidou, I., Phaethon, A System for the Validation of Satellite Derived Atmospheric Columns of Trace Gases, in Advances in Meteorology, Climatology and Atmospheric Physics, edited by C. G. Helmis and P. T. Nastos, pp. 1081-1088, Springer Berlin Heidelberg, 10.1007/978-3-642-29172-2_151, 2013.

Kramer, L. J., R. J. Leigh, J. J. Remedios, and P. S. Monks, Comparison of OMI and ground-based in situ and MAX-DOAS measurements of tropospheric nitrogen dioxide in an urban area, J. Geophys. Res., 113, D16S39, doi:10.1029/2007JD009168, 2008.

Kuenen J, van der Gon HD, Visschedijk A, Dröge R, van Gijlswijk R., MACC European emission inventory for the years 2003-2007. The Netherlands Organisation report, TNO-060-UT-2011-00588, 2011.

Kukkonen, J., Balk, T., Schultz, D.M., Baklanov, A., Klein, T., Miranda, A I., Monteiro, A., Hirtl, M., Tarvainen, V., Boy, M., Peuch, V.-H., Poupkou, A., Kioutsioukis, I., Finardi, S., Sofiev, M., Sokhi, R.S., Lehtinen, K., Karatzas, K., San Jose, R., Astitha, M., Kallos, G., Schaap, M.M., Reimer, E., Jakobs. H. and Eben, K., "A review of operational, regional-scale, chemical weather forecasting models in Europe", Atmospheric Chemistry and Physics, 12, pp. 1–87, 2012.

Lambert, J.-C., G. Pinardi, J. Granville, K. Clemer, A. DelCloo, P. Valks, and N. Hao, O3MSAF validation report, AF/O3M/IASB/VR/NO2/095Rep, 2011.

Lamsal et al., L.N., R.V. Martin, A. van Donkelaar, E.A. Celarier, E.J. Bucsela, K.F. Boersma, R.D.C. Luo, Y. Wang, Indirect validation of tropospheric nitrogen dioxide retrieved from the OMI satellite instrument: insight into the seasonal variation

of nitrogen oxides at northern midlatitudes, J. Geophys. Res., 115, p. D05302 http://dx.doi.org/10.1029/2009JD013351, 2010.

Lee, D. S., Kohler, I., Grobler, E., Rohrer, F., Sausen, R., Gallardo-Klenner, L., Olivier, J. G. J., Dentener, F. J., and Bouwman, A. F.: Estimations of global NOx emissions and their uncertainties, Atmos. Environ., 31, 1735–1749, 1997.

Lee S. M., M. Princevac, S. Mitsutomi, and J. Cassmassi, "MM5 simulations for air quality modeling: an application to a coastal area with complex terrain," Atmospheric Environment, vol. 43, no. 2, pp. 447–457, 2009.

Lei, W., de Foy, B., Zavala, M., Volkamer, R., and Molina, L. T.: Characterizing ozone production in the Mexico City Metropolitan Area: a case study using a chemical transport model, Atmos. Chem. Phys., 7, 1347-1366, doi:10.5194/acp-7-1347-2007, 2007.

Levelt, P. F., G. H. J. van den Oord, M. R. Dobber, A. Ma¨lkki, H. Visser, J. de Vries, P. Stammes, J. Lundell, and H. Saari, The Ozone Monitoring Instrument, IEEE Trans. Geosci. Remote Sens., 44(5), 1093–1101, doi:10.1109/TGRS.2006.872333, 2006.

Li, X., Brauers, T., Hofzumahaus, A., Lu, K., Li, Y. P., Shao, M., Wagner, T., and Wahner, A.: MAX-DOAS measurements of NO2, HCHO and CHOCHO at a rural site in Southern China, Atmos. Chem. Phys., 13, 2133-2151, doi:10.5194/acp-13-2133-2013, 2013.

Liora, N., Markakis, K., Poupkou, A., Giannaros, Th., Melas, D., The Natural Emissions Model (NEMO): Description, application and model evaluation. Atmospheric Environment (2015) 122C, pp. 493-504,doi:10.1016/j.atmosenv.2015.10.014, 2015.

Liora, N., Poupkou, A., Giannaros, T.M. Kakosimos, K.E., Stein, O. and Melas, D., Impacts of natural emission sources on particle pollution levels in Europe, Atmospheric Environment, 137. pp. 171-185, 2016.

Loyola D., Thomas W., Livschitz Y., Ruppert T., Albert P.,and Hollmann R., Cloud properties derived from GOME/ERS-2 backscatter data for trace gas retrieval, IEEE Transactions in Geoscience and Remote Sensing, vol. 45, no. 9, pp. 2747-2758, 2007.

Ma, J. Z., Beirle, S., Jin, J. L., Shaiganfar, R., Yan, P., and Wagner, T.: Tropospheric NO_2 vertical column densities over Beijing: results of the first three years of ground-based MAX-DOAS measurements (2008–2011) and satellite validation, Atmos. Chem. Phys., 13, 1547-1567, doi:10.5194/acp-13-1547-2013, 2013.

Marchenko, S., Krotkov, N. A., Lamsal, L. N., Celarier, E. A., Swartz, W. H., and Bucsela, E. J.: Revising the slant column density retrieval of nitrogen dioxide observed by the Ozone Monitoring Instrument, J. Geophys. Res.-Atmos., 120, 1–23, doi:10.1002/2014JD022913, 2015.

Markakis, K., Katragkou, E., Poupkou, A. and Melas, D., "MOSESS: A new emission model for the compilation of model-ready emission inventories. Application in a coal mining area in Northern Greece", Environmental Modeling & Assessment, 18, pp. 509–521, 2013.

Mayer, B. and Kylling, A.: Technical note: The libRadtran software package for radiative transfer calculations – description and examples of use, Atmos. Chem. Phys., 5, 1855–1877, doi: 10.5194/acp-5-1855-2005, 2005.

Moussiopoulos N., Vlachokostas Ch., Tsilingiridis G., Douros I., Hourdakis E., Naneris C., Sidiropoulos C., Air quality status in Greater Thessaloniki Area and the emission re-ductions needed for attaining the EU air quality legislation. Science of the Total Environ-ment 407:1268-1285. doi:10.1016/j.scitotenv.2008.10.034Noxon, J.F. Nitrogen dioxide in the stratosphere and troposphere measured by ground-based absorption spectroscopy. Science 1975, 189, 547–549, 2008.

Nevas S., J. Gröbner, L. Egli, and M. Blumthaler, "Stray light correction of array spectroradiometers for solar UV measurements," Appl. Opt. 53, 4313-4319, 2014.

Noxon, J.F. Nitrogen dioxide in the stratosphere and troposphere measured by ground-based absorption spectroscopy. Science 1975, 189, 547–549.

OrdóñEz, C., A. Richter, M. Steinbacher, C. Zellweger, H. Nüß, J. P. Burrows, and A. S. H. Prevôt, Comparison of 7 years of satellite-borne and ground-based tropospheric NO2 measurements around Milan, Italy, J. Geophys. Res., 111, D05310, doi:10.1029/2005JD006305, 2006.

Ozone Monitoring Instrument (OMI) Data User's Guide, 2012, available at http://disc.sci.gsfc.nasa.gov/Aura/additional/documentation/README.OMI_DUG.pdf

Palmer, P. I., Jacob, D. J., Chance, K., Martin, R. V., Spurr, R. J. D., Kurosu, T. P., Bey, I., Yantosca, R., Fiore, A., and Li, Q.: Airmass factor formulation for spectroscopic measurements from satellites: application to formaldehyde retrievals from GOME, J. Geophys. Res., 106, 14539–14550, 2001.

Poupkou, A., Giannaros, T., Markakis, K. Kioutsioukis, I., Curci, G., Melas, D., and Zerefos, C., "A model for European biogenic volatile organic compound emissions: Software development and first validation", Environmental Modelling and Software, 25, pp. 1845-1856, 2010.

Poupkou, A., Nastos, P., Melas, D. and Zerefos, C., "Climatology of Discomfort Index and Air Quality Index in a large urban Mediterranean agglomeration", Water, Air &Soil Pollution, 222, pp. 163–183, 2011.

Poupkou, A., Markakis, K., Liora, N., Giannaros, T., Zanis P., Im, U., Daskalakis, N., Myriokefalitakis, S., Kaiser, J. W., Melas, D., Kanakidou, M., Karacostas, T. and Zerefos, C., "A modeling study of the impact of the 2007 Greek forest fires on the gaseous pollutant levels in the Eastern Mediterranean", Atmospheric Research, 148, pp. 1-17, 2014.

Platt, U.: Differential optical absorption spectroscopy (DOAS), in Air Monitoring by Spectroscopic Techniques, Chem. Anal. Ser., 127, 27–84, John Wiley, New York, 27–84, 1994.

Platt, U. and Stutz, J.: Differential Optical Absorption Spectroscopy, Principles and Applications, Springer, Physics of Earth and Space Environments, ISBN 978-3-540-21193-8, 2008.

Resident Population Census 2011. Hellenic Statistical Authority web site. URL: http://www.statistics.gr/en/home. Last visited August 2016.

Richter, A., Godin, S., Gomez, L., Hendrick, F., Hocke, K., Langerock, B., van Roozendael, M., and Wagner, T.: Spatial Representativeness of NORS observations, Report, 1 November 2013.

Rothman L.S., A. Barbe, D.Chris Benner et al., "The HITRAN molecular spectroscopic database: Edition of 2000 including updates through 2001", Journal of Quantitative Spectroscopy and Radiative Transfer 82, 5-44, 2003.

Seinfeld, J. H. and Pandis, S. N.: Atmospheric Chemistry and Physics: From Air Pollution to Climate Change, J. Wiley, New York, 1998.

Skamarock W.C., Klemp J.B., Dudhia J., Gill D.O., Barker D.M., Duda M.G., Huang X.Y., Wang W., Powers J.G., A description of the advanced research WRF version 3. NCAR Technical Note (NCAR/TN – 475 + STR), Boulder, Colorado, USA, 2008.

Solomon, S., Portmann, R., Sandres,W., et al.: On the role of nitrogen dioxide in the absorption of solar radiation, J. Geophys. Res. 104(D10), 12047–12058, 1999.

Spurr, R. J. D., T. P. Kurosu, and K. V. Chance, A Linearized Discrete Ordinate Radiative Transfer Model for Atmospheric Remote Sensing Retrieval, J. Quant. Spectrosc. Radiat. Transfer, 68, 689-735, 2001.

Spurr R.J.D., Van Roozendael M., Loyola D.G., "Algorithm Theoretical Basis Document for GOME Total Column Densities of Ozone and Nitrogen Dioxide. P/GDOAS: GDP 4.0", ERSE-DTEXEOPG- TN-04-0007, Iss./Rev.:1/A, 2004.

Spurr, R.: LIDORT and VLIDORT: Linearized pseudo-spherical scalar and vector discrete ordiate radiative transfer models for use in remote sensing retrieval problems. Light Scattering Reviews, Volume 3, edited by: Kokhanovsky, A., Springer, 2008.

Tewari M., Chen F., Wang W., Dudhia J., LeMone M.A., Mitchell K., Ek M., Gayno G., Wegiel J., Cuenca R.H., Implementation and verification of the unified NOAH land surface model in the WRF model. *20th conference on weather analysis and forecasting/16th conference on numerical weather prediction*, pp. 11–15, 2004.

Thompson G., Paul R.F., Roy M.R., William D.H., Explicit Forecasts of Winter Precipitation Using an Improved Bulk Microphysics Scheme. Part II: Implementation of a New Snow Parameterization. *Mon. Wea. Rev.*, **136**, 5095–5115, 2008.

Valks, P., Pinardi, G., Richter, A., Lambert, J.-C., Hao, N., Loyola, D., Van Roozendael, M., and Emmadi, S.: Operational total and tropospheric NO2 column retrieval for GOME-2, Atmos. Meas. Tech., 4, 1491–1514, doi:10.5194/amt-4-1491-2011, 2011.

Van der A, R. J., Eskes, H. J., Boersma, K. F., et al.: Trends, seasonal variability and dominant NOx source derived from a ten year record of NO_2 measured from space, J. Geophys. Res., 113, D04302, doi:10.1029/2007JD009021, 2008.

Vandaele A.C., C. Hermans, P.C. Simon, M. Carleer, R. Colins, S. Fally, M.F. Mérienne, A. Jenouvrier, and B. Coquart, "Measurements of the NO2 absorption cross-sections from 42000 cm-1 to 10000 cm-1 (238-1000 nm) at 220 K and 294 K," J. Quant. Spectrosc. Radiat. Transfer 59, 171-184, 1998.

Wagner, T., B. Dix, C. v. Friedeburg, U. Frieß, S. Sanghavi, R. Sinreich, and U. Platt, MAX-DOAS O4 measurements: A new technique to derive information on atmospheric aerosols—Principles and information content, J. Geophys. Res., 109, D22205, doi:10.1029/2004JD004904, 2004.

Wallace, J., Kanaroglou, P., The sensitivity of OMI-derived nitrogen dioxide to boundary layer temperature inversions, Atmospheric Environment, Volume 43, Issue 22, p. 3596-3604, 2009.

Wenig, M., Kuhl, S., Beirle, S., Bucsela, E., Jahne, B., Platt, U., Gleason, J., and Wagner, T.: Retrieval and analysis of stratospheric NO2 from the Global Ozone Monitoring Experiment, J. Geophys. Res., 109, D04315, doi:10.1029/2003JD003652, 2004.

Wenig, M. O., Cede, A. M., Bucsela, E. J., Celarier, E. A., Boersma, K. F., Veefkind, J. P., Brinksma, E. J., Gleason, J. F., and Herman, J. R.: Validation of OMI tropospheric NO2 column densities using direct-sun mode Brewer measurements at NASA Goddard Space Flight Center, J. Geophys. Res., 113, D16S45, doi:10.1029/2007JD008988, 2008.

Yarwood G., Rao S., Yocke M., Whitten G.Z., Updates to the Carbon Bond chemical mechanism: CB05. Final Report prepared for US EPA, RT-04-00675 (http://www.camx.com/publ/pdfs/CB05_Final_Report_120805.pdf), 2005.

Zyrichidou, I., Koukouli, M. E., Balis, D. S., Katragkou, E., Melas, D., Poupkou, A., Kioutsioukis, I., van der A, R., Boersma, F. K., van Roozendael, M. and Richter, A., "Satellite observations and model simulations of tropospheric NO_2 columns over south-eastern Europe", Atmospheric Chemistry and Physics, 9, pp. 6119–6134, 2009.

Zyrichidou I., Koukouli M. E., Balis D., Kioutsioukis I., Poupkou A., Katragkou E., Melas D., Boersma F. and van Roozendael M., "Evaluation of high resolution simulated and OMI retrieved tropospheric NO_2 column densities over Southeastern Europe", Atmospheric Research, 122, pp. 55-66, 2013.

Zyrichidou I., M. E. Koukouli, D. Balis, K. Markakis, I. Kioutsioukis , A. Poupkou, D. Melas, K.F. Boersma & M. van Roozendael, Identification of surface NOx emission sources on a regional scale using OMI NO_2, Atmospheric Environment, 101, 82-93, 2015.

Zyryanov, D., Foret, G., Eremenko, M., Beekmann, M., Cammas, J.-P., D'Isidoro, M., Elbern, H., Flemming, J., Friese, E., Kioutsioukis, I., Maurizio, A., Melas, D., Meleux, F., Menut, L., Moinat, P., Peuch, V.-H., Poupkou, A., Razinger, M., Schulz, M., Stein, O., Suttie, A.M., Valdebenito, A., Zerefos, C., Dufour, G., Bergametti G. and Flaud, J.-M., "3-D evaluation of tropospheric ozone simulations by an ensemble of regional Chemistry Transport Model", Atmospheric Chemistry and Physics, 12, pp. 3219-3240, 2012.

Table 1. Information on campaign locations and measurements performed there.

	LAP-AUTH (UC)	ATEITH (SC)	Epanomi (RC)
Air quality conditions	Urban	Sub-urban/Industrial	Rural
Latitude	40.63N	40.65N	40.37N
Longitude	22.96E	22.81E	22.98E
System	Phaethon #1	Phaethon #3	Phaethon #2
Period of operation	1/11/2014 - 11/5/2015	20/1/2015 - 11/5/2015	1/11/2014 - 31/1/2015
Number of NO_2 trop. VCD measurements	7930	16716	5738

Table 2. Tropospheric NO_2 ~~S~~statistics from the comparison of Phaethon #2 and #3 systems to Phaethon #1 during the period 11 - 1~~98~~ October 2014. The hourly averaged vertical columns at both 15° and 30° elevation viewing angles are compared.

	Phaethon #2	Phaethon #3
Number of observations	75	75
Correlation coefficient (r)	0.95	0.92
Slope of the linear fit	1.03	1.07
Mean bias [$x10^{15}$ molec. cm^{-2}]	0.58	0.73
Standard deviation (1σ) [$x10^{15}$ molec. cm^{-2}]	2.51	3.12

Table 3: Main features of the satellite algorithms.

	DLR GDP 4.7 (GOME2)	NASA V3 (OMI)
SCD Retrieval Methodology	DOAS within 425-450nm [Platt, 1994; Platt and Stutz, 2008]	DOAS within 402-465nm [Marchenko et al., 2015]
Stratospheric component	Spatial filtering [Wenig et al., 2004] / masking of polluted areas [Loyola et al., 2007; Valks et al., 2011]	In regions of tropospheric pollution, stratospheric column is inferred using a local analysis of the stratospheric field [Celarier et al.,2008; Bucsela et al., 2013]
Cloud algorithm	OCRA/ROCINN version 2.0 [Loyola et al., 2007]	Updated O_2–O_2 [Acarreta et al., 2004]
AMF calculation	LUT generated using the Linearized Discrete Ordinate Radiative Transfer (LIDORT) Model [Palmer et al., 2001; Spurr et al., 2001; 2008]	LIDORT Model [Palmer et al., 2001; Spurr et al., 2001; 2008]
NO_2 a-priori profile	Monthly mean profiles derived from MOZART -2 CTM [Horowitz et al., 2003]	Monthly mean profiles derived from Global Modeling Initiative CTM [Douglass et al., 2004]
Main algorithm reference	Valks et al. [2011] or Hassinen et al. [2015]	Celarier et al. [2008], Bucsela et al. [2013; 2016]

Table ~~3~~4. Average and standard deviation of space-borne and ground-based tropospheric NO_2 observations over each campaign location. Phaethon mean values have been calculated from measurements at 15° and 30° elevation viewing angles (see also section 2.2) within ±30 min around the satellite overpass time.

NO_2 trop. VCD mean (±1σ) [x10^{15} molec. cm^{-2}] from	RC site	SC site	UC site
OMI	3.39 (± 1.40)	2.08 (± 1.24)	3.17 (± 2.30)
Phaethon (OMI overpass time)	4.73 (± 2.42)	2.71 (± 1.37)	11.35 (±8.51)
GOME2A	3.04 (± 1.58)	2.17 (± 1.25)	2.93 (± 1.47)
Phaethon (GOME2A overpass time)	4.30 (± 1.63)	4.77 (± 3.03)	13.44 (± 8.62)
GOME2B	3.33 (± 2.50)	2.35 (± 1.19)	2.87 (± 1.75)
Phaethon (GOME2B overpass time)	5.70 (± 2.23)	4.66 (± 2.84)	13.08 (± 9.04)

Table 54. Statistics from the comparison of space-borne and ground-based NO_2 tropospheric VCDs for each campaign location. The same MAX-DOAS data were used as in Table 4.

	Compared to Phaethon NO_2 trop. VCD	RC site	SC site	UC site
OMI	Number of collocations	14	26	30
	Correlation coefficient (r)	0.31	0.52	0.63
	Slope	0.18	0.47	0.17
	Intercept [$x10^{15}$ molec. cm^{-2}]	2.54	0.82	1.25
	Mean bias [$x10^{15}$ molec. cm^{-2}]	-1.34	-0.63	-8.18
	Standard deviation (1σ) [$x10^{15}$ molec. cm^{-2}]	2.39	1.29	7.29
GOME2A	Number of collocations	22	34	39
	Correlation coefficient (r)	0.44	0.02	0.28
	Slope	0.42	0.01	0.05
	Intercept [$x10^{15}$ molec. cm^{-2}]	1.22	2.12	2.28
	Mean bias [$x10^{15}$ molec/cm^2]	-1.26	-2.60	-10.51
	Standard deviation (1σ) [$x10^{15}$ molec. cm^{-2}]	1.70	3.25	8.32
GOME2B	Number of collocations	27	52	55
	Correlation coefficient (r)	-0.10	-0.07	0.19
	Slope	-0.11	-0.03	0.04
	Intercept [$x10^{15}$ molec. cm^{-2}]	3.97	2.48	2.39
	Mean bias [$x10^{15}$ molec/cm^2]	-2.37	-2.31	-10.21
	Standard deviation (1σ) [$x10^{15}$ molec. cm^{-2}]	3.51	3.16	8.87

Table 6~~5~~. Average and standard deviation of the CAMx simulated NO_2 tropospheric VCDs for each campaign location during the entire period of the campaign, for the 2×2 km^2 grid of each monitoring site ~~(2×2 km^2),~~ ~~and~~ for the OMI nadir pixel size (14x26 km^2) and the corresponding mean ratios. The ratios estimated using only the NO_2 columns corresponding to the OMI overpass time have been used as adjustment factors for the reconstruction of the OMI observations. Also, the ratios using two and three model cells in the light path direction are presented.

Mean (±1σ) NO_2 trop. VCDs [x10^{15} molec. cm^{-2}] and adjustment factors from		RC site	SC site	UC site
All simulations	2x2 km^2	3.70 (±2.74)	5.02 (±3.73)	11.58 (±8.43)
	14x26 km^2	3.59 (±2.37)	5.73 (±3.22)	5.87 (±3.36)
	Ratio	1.00 (±0.16)	0.85 (±0.25)	1.91 (±0.75)
	Ratio (2 cells)	1.00 (±0.16)	0.83 (±0.23)	1.93 (±0.66)
	Ratio (3 cells)	1.00 (±0.15)	0.81 (±0.21)	1.83 (±0.60)
Simulations near OMI overpass time	2x2 km^2	2.85 (±1.97)	3.62 (±2.64)	12.43 (±8.66)
	14x26 km^2	2.85 (±1.55)	4.50 (±2.36)	5.46 (±3.12)
	Ratio	0.96 (±0.18)	0.78 (±0.24)	2.20 (±0.75)
	Ratio (2 cells)	0.95 (±0.18)	0.77 (±0.23)	2.09 (±0.66)
	Ratio (3 cells)	0.94 (±0.17)	0.76 (±0.22)	1.92 (±0.62)

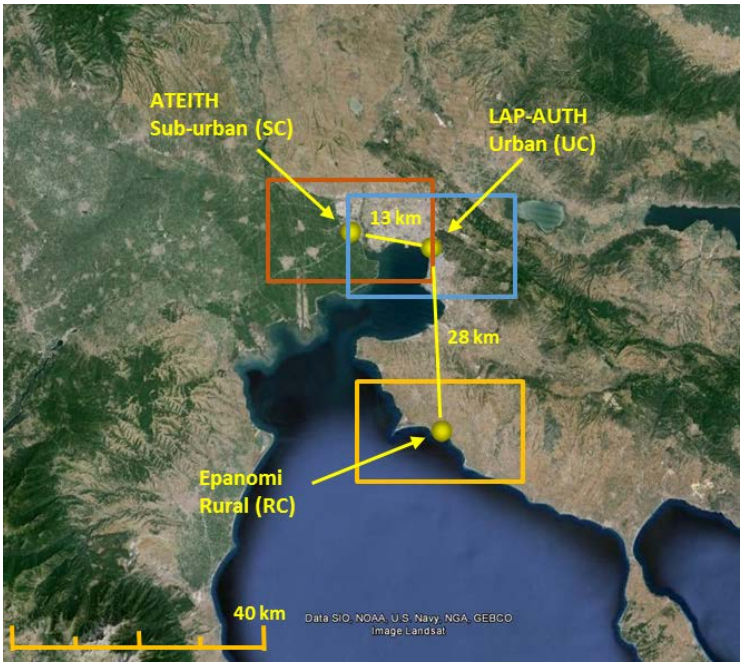

Figure 1: Map of the greater Thessaloniki area with the three sites of measurements: UC (blue), SC (red) and RC (yellow). The rectangular outlines represent the area covered by the nadir pixel size of OMI centered at each location (Courtesy of Google Earth NASA Images).

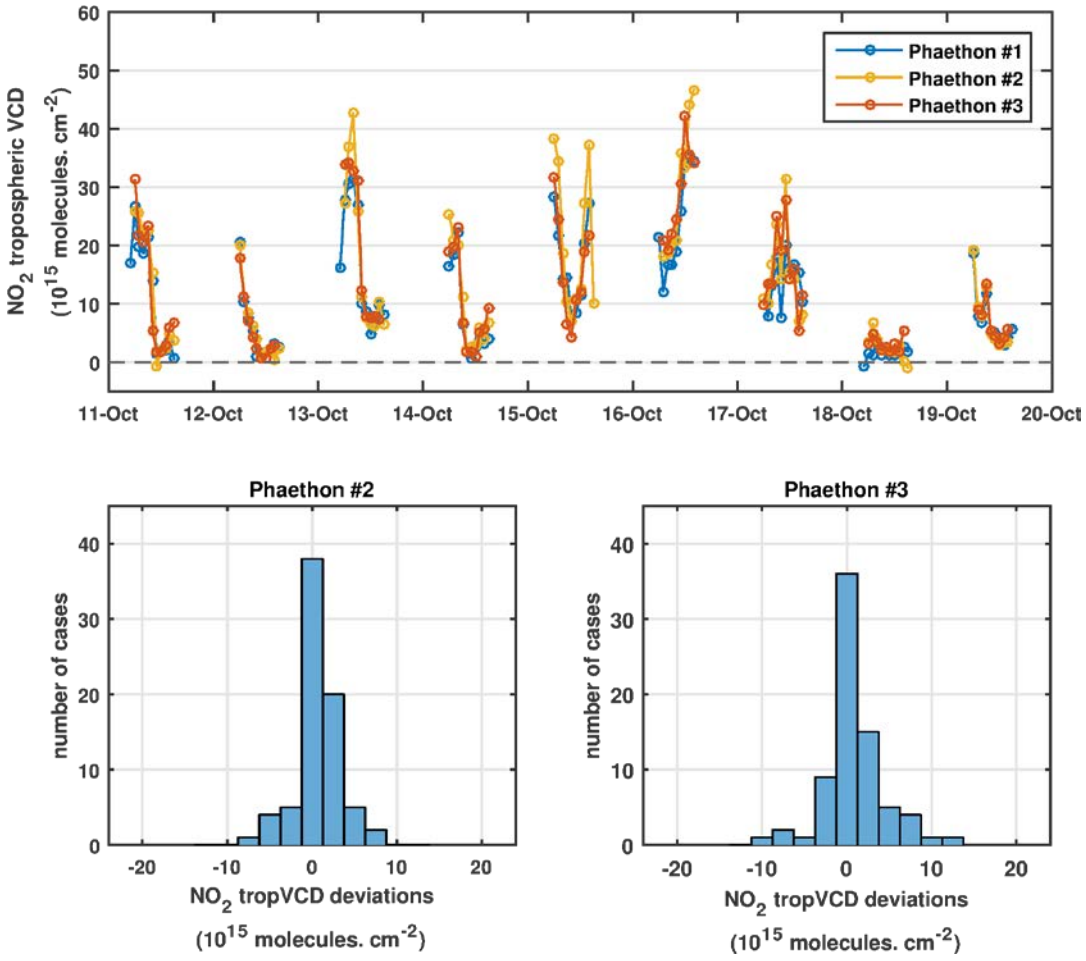

Figure 2: The Phaethon systems were operating in parallel in the University Campus from 11 to 19 October 2014. Upper panel: Hourly mean NO_2 tropospheric VCD time series of the three systems retrieved for 15° and 30° elevation angles. Lower panels: Histograms of the NO_2 tropospheric VCD differences of Phaethon #2 and #3 relative to Phaethon #1.~~Histograms of the NO_2 tropospheric VCD differences of Phaethon #2 and #3 relative to Phaethon #1. The three systems were operating in parallel in the University Campus for 8 days, from 11 to 18 October 2014.~~

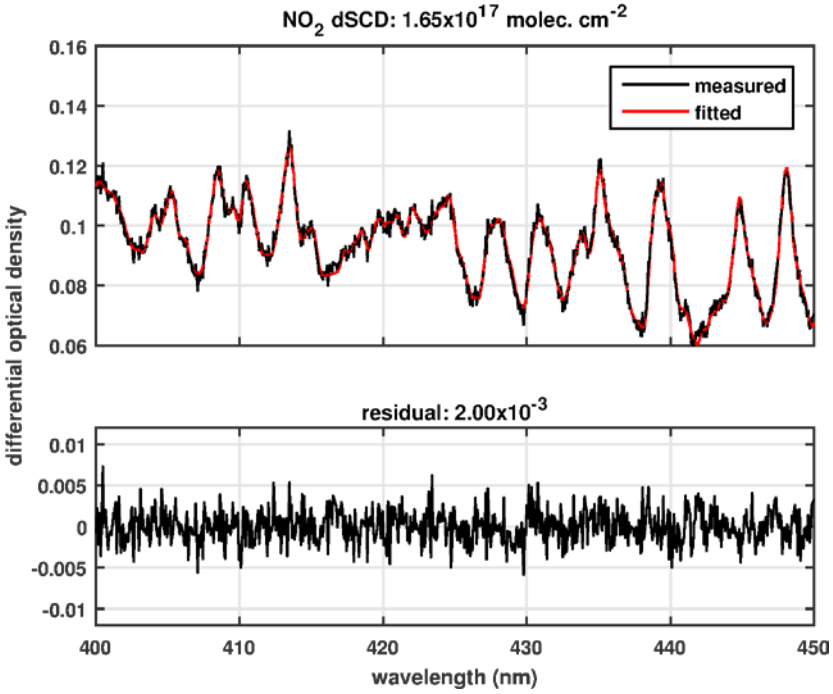

Figure 3: Example of NO_2 fitting results obtained at the UC site on 6 November 2014, around 10:30 UTC, at an elevation angle of 5° and a SZA ~57°. The upper panel shows the measured (black) and the fitted (red) NO_2, and the lower panel shows the residual of the DOAS fit.

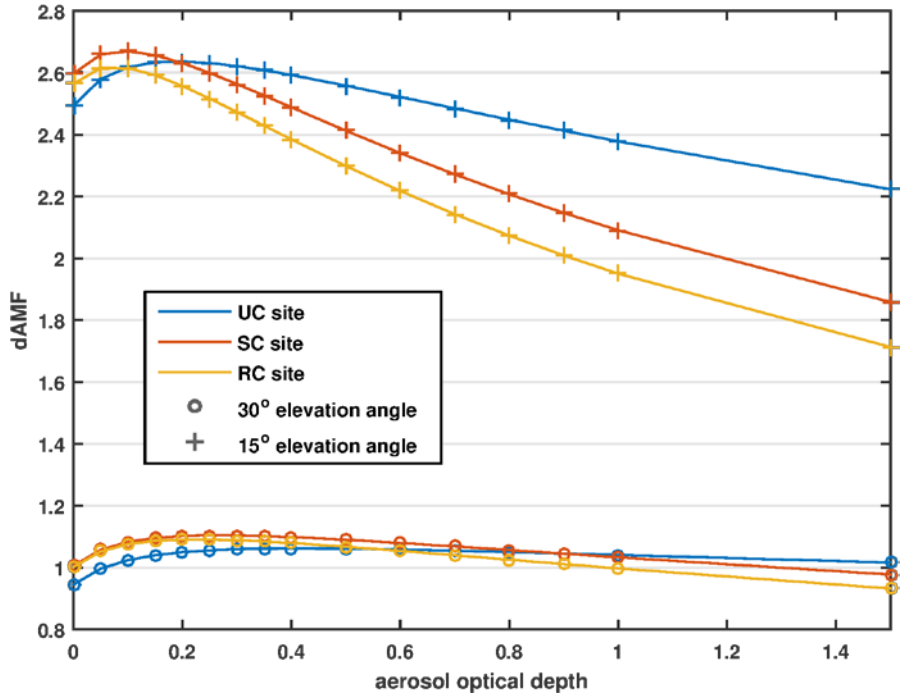

Figure 4: Example of AMFs calculated with libRadtran at SZA 40º and azimuth angle ~~100º~~ 80º relative to the sun for each campaign site. The AMFs at 15º (crosses) and 30º (circles) elevation angles are plotted versus the AOD.

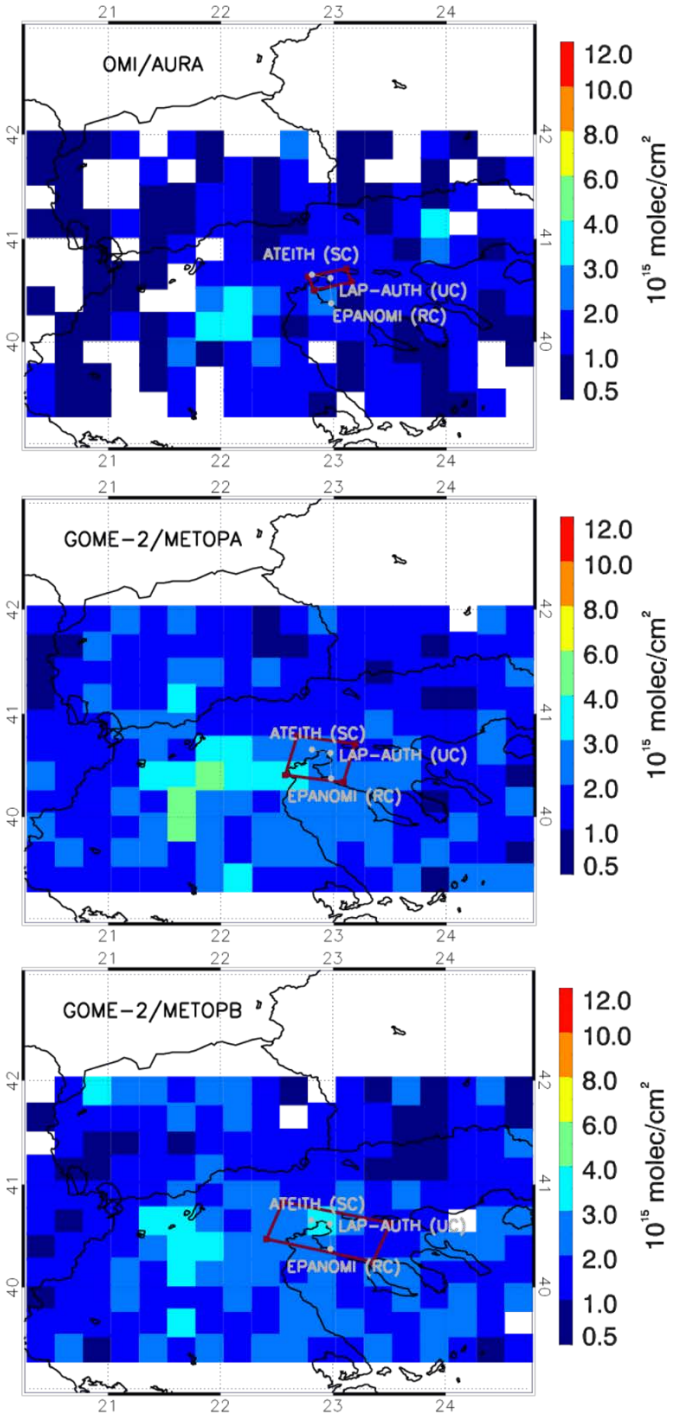

Figure 5: Maps of the tropospheric NO_2 spatial distribution averaged over the campaign period from OMI (upper panel), GOME2A (middle panel) and GOME2B (lower panel) observations. The dark red outlined areas represent the GOME-2 and OMI pixel sizes for the 11th and 12th of November 2014, respectively. Blank cells indicate lack of sufficiently good quality data.

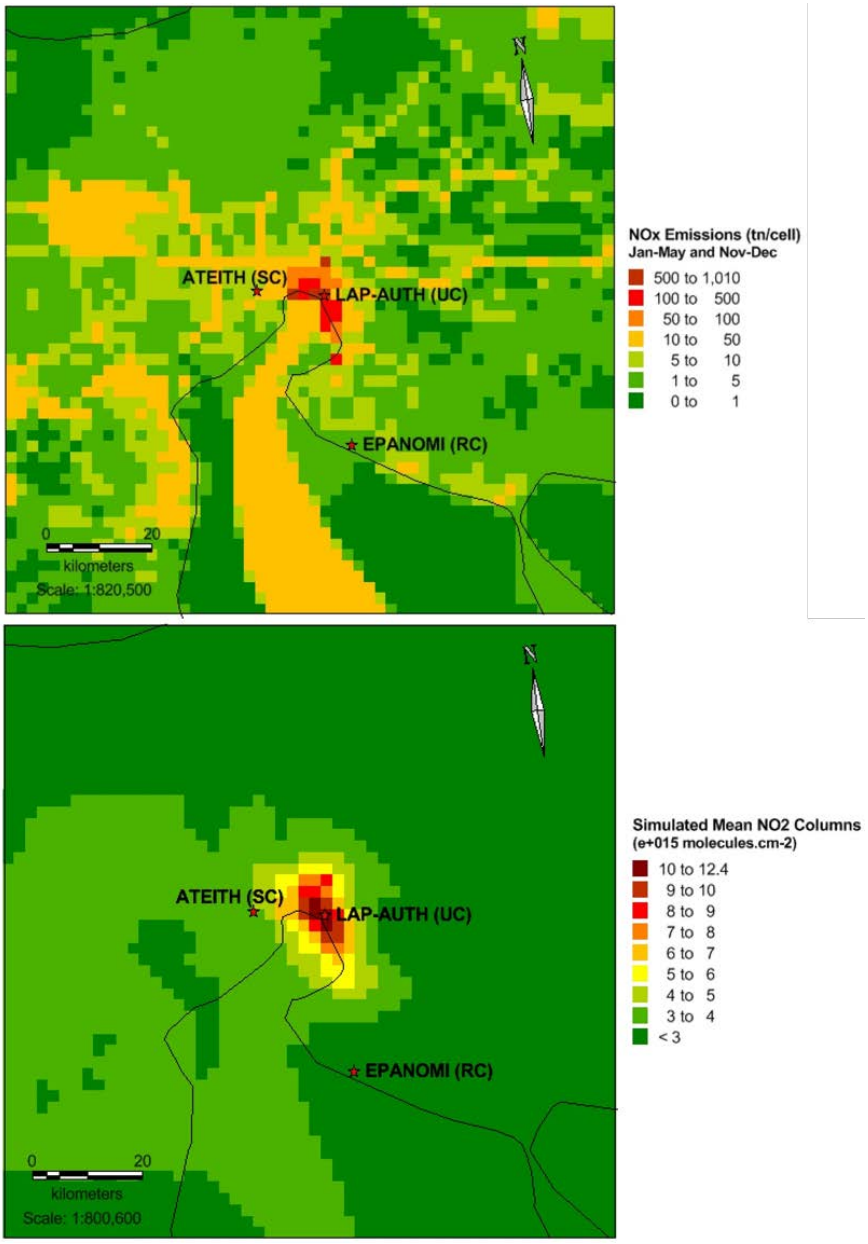

Figure 6~~5~~: The upper panel shows the total NOx emissions of the period November to May for the domain of Thessaloniki. ~~The upper panel shows the NOx emissions for the domain of Thessaloniki during the months included in the period of the campaign (November 2014 – May 2015)~~. The lower panel shows ~~For the framed area~~ the simulated NO_2 VCD averaged over the period of the campaign for the same domain. ~~is presented for each cell within the OMI footprint over the three campaign sites (lower panel).~~

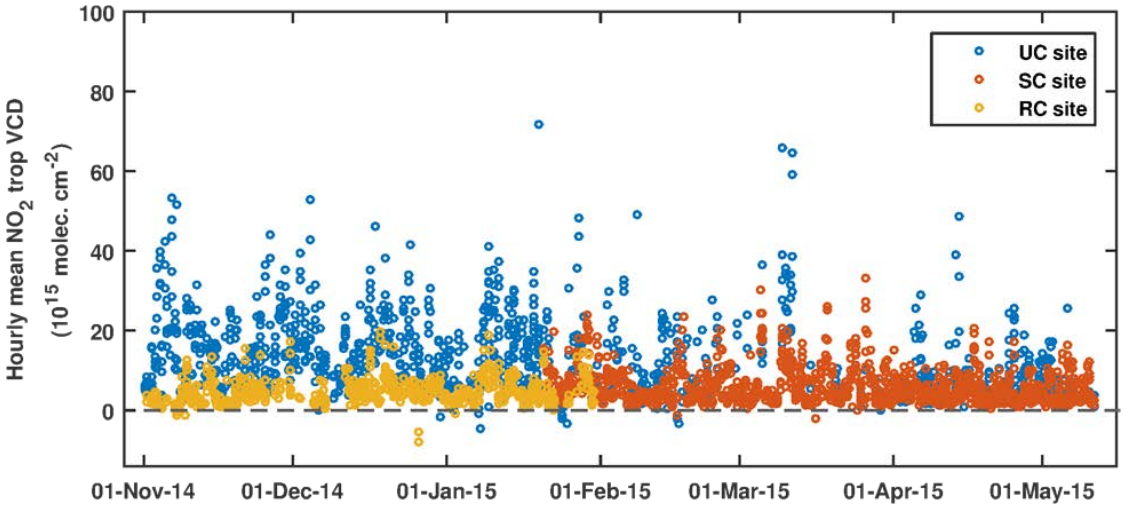

Figure 7~~6~~: Time series of hourly mean tropospheric NO_2 ~~column~~ VCD measurements performed at 15° and 30° elevation angles by Phaethon at the three campaign sites.

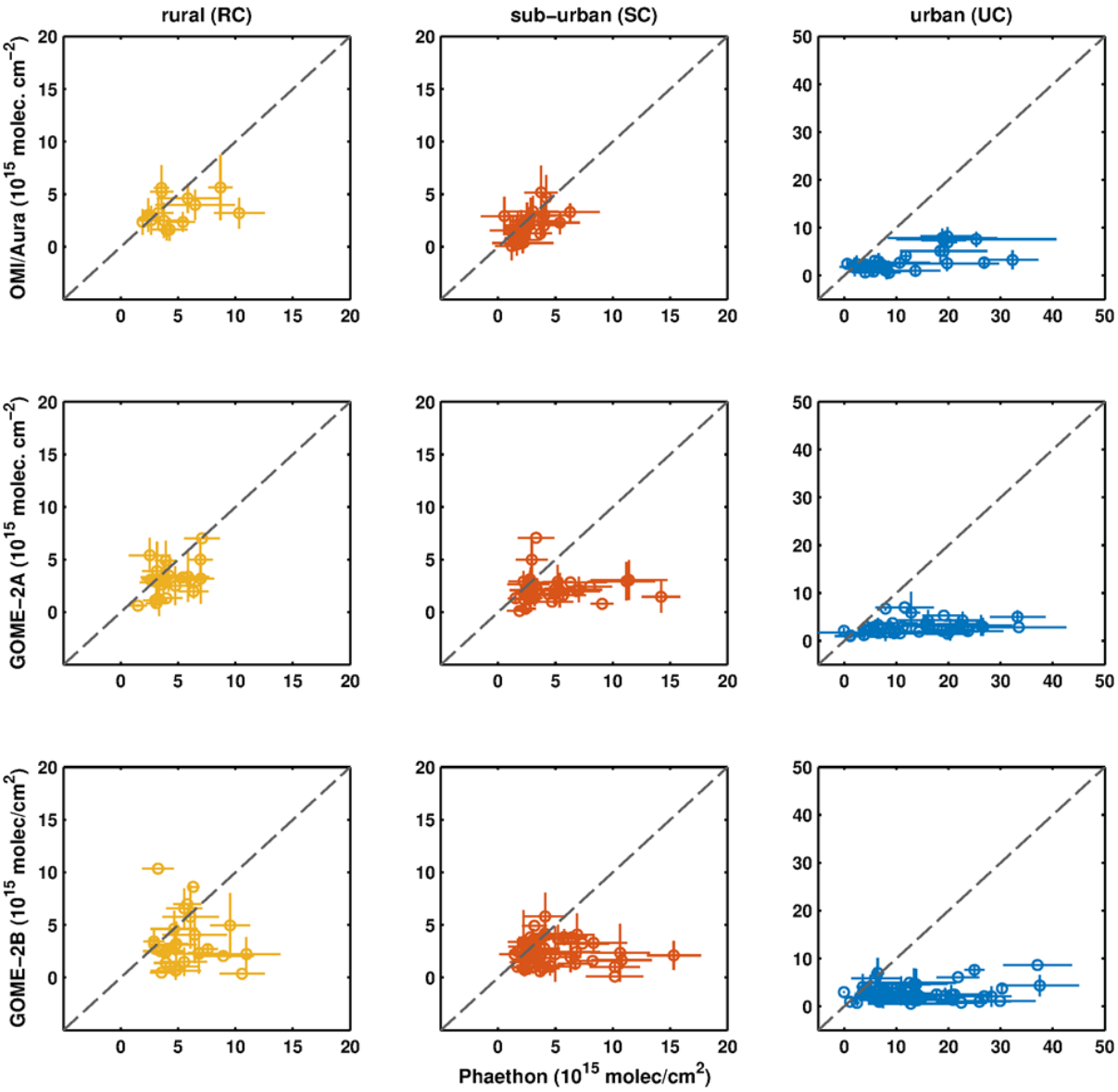

Figure ~~87~~: Scatter plots of tropospheric NO_2 VCD derived from the ground and space for each campaign site (RC left column, SC middle column, and UC right column) and satellite sensor (OMI top row, GOME2A middle row and GOME2B bottom row). Error bars are the standard deviation of all data points entering the mean for the ground-based data and the estimated total error for the satellite overpass data. Statistics from the comparisons can be found in table 4.

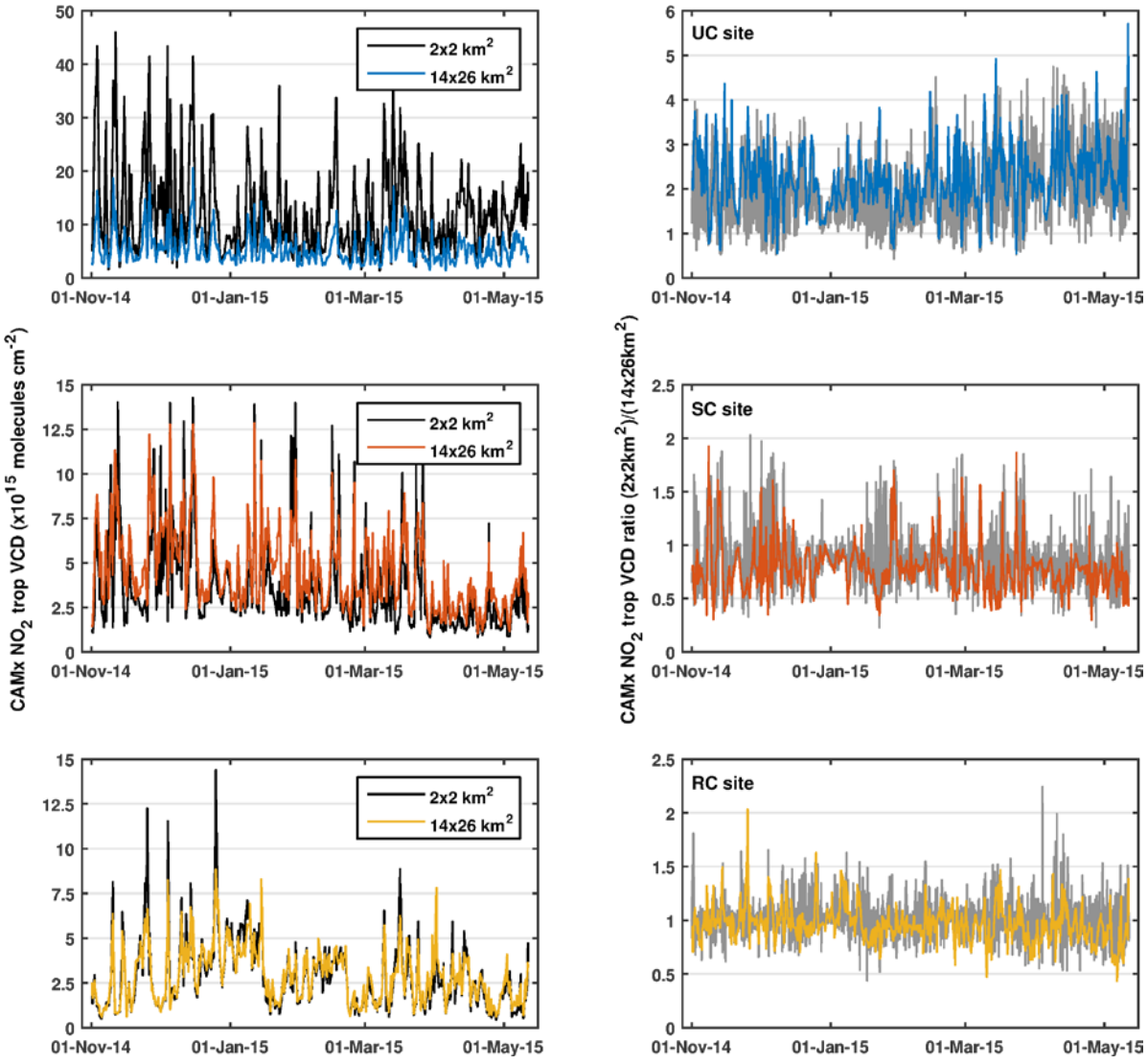

Figure ~~9~~8: Hourly NO_2 tropospheric VCDs (left column) and the adjustment factors (right column) calculated by means of CAMx air quality simulations for the UC site (top row), the SC site (middle row) and the RC site (bottom row). Left panels: Only the NO_2 columns from CAMx corresponding to OMI overpass time are presented here. The black lines correspond to an area of 2x2 km^2 which includes each site and the colored lines to the OMI nadir pixel size area. Right panels: The adjustment factors (ratios) calculated using all the hourly modelled NO_2 columns are presented in grey while in color are the simulations corresponding to OMI overpass time.

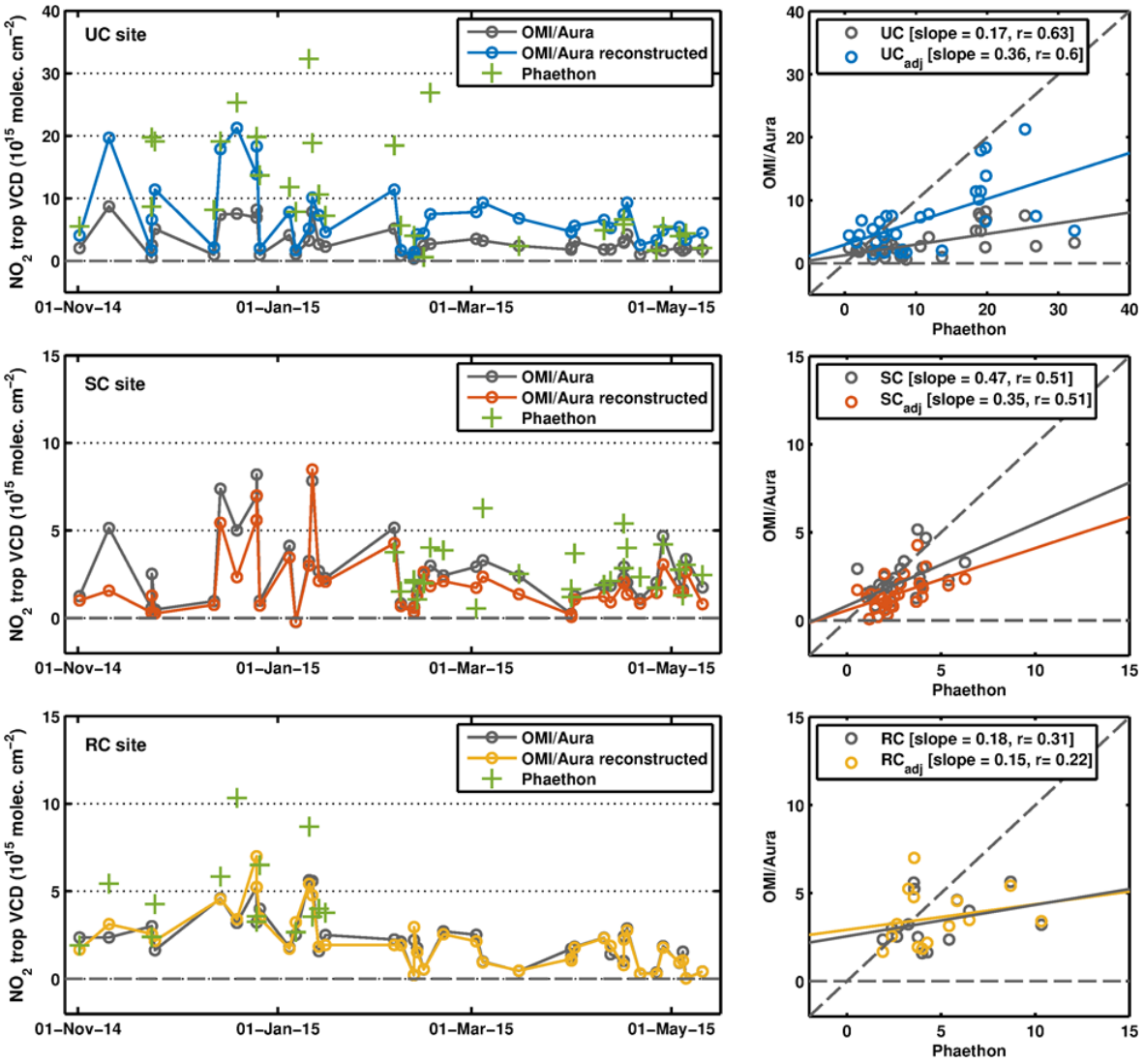

Figure 10~~9~~: Time series of tropospheric NO_2 derived from Phaethon and OMI before and after the adjustment with CAMx simulations is applied (left panels). The corresponding scatter plots are shown in the right panels.